

Distinct Contribution of Adult-Born Hippocampal Granule Cells to Context Encoding

Highlights

- Ca^{2+} imaging of DG GCs *in vivo* indicates abGCs are more active than mGCs
- abGCs are less spatially tuned than mGCs
- Spatially tuned mGCs and abGCs remap spatial representations to a similar degree
- abGCs actively participate in the encoding of novel information

Authors

Nathan B. Danielson, Patrick Kaifosh,
Jeffrey D. Zaremba, ..., René Hen,
Attila Losonczy, Mazen A. Kheirbek

Correspondence

al2856@cumc.columbia.edu

In Brief

Danielson et al. monitored and controlled the activity of adult-born and mature dentate gyrus neurons *in vivo*. They show that as a population, young adult-born neurons are more active and less sharply spatially tuned than their mature counterparts and that these cells contribute to context encoding.

Distinct Contribution of Adult-Born Hippocampal Granule Cells to Context Encoding

Nathan B. Danielson,^{3,4} Patrick Kaifosh,^{3,4} Jeffrey D. Zaremba,^{3,4} Matthew Lovett-Barron,^{3,6} Joseph Tsai,^{3,4} Christine A. Denny,^{1,2} Elizabeth M. Balough,^{3,4} Alexander R. Goldberg,² Liam J. Drew,^{1,2,7} René Hen,^{1,2,3,5} Attila Losonczy,^{3,5,*} and Mazen A. Kheirbek^{1,2,8,9}

¹Department of Psychiatry, Columbia University, New York, NY 10032, USA

²Division of Integrative Neuroscience, New York State Psychiatric Institute, New York, NY 10032, USA

³Department of Neuroscience

⁴Doctoral Program in Neurobiology and Behavior

⁵Kavli Institute for Brain Science

Columbia University, New York, NY 10032, USA

⁶Department of Bioengineering, Stanford University, Stanford, CA 94305, USA

⁷Wolfson Institute for Biomedical Research, UCL, London WC1E 0BT, UK

⁸Department of Psychiatry

⁹Center for Integrative Neuroscience

University of California, San Francisco, San Francisco, CA 94158, USA

*Correspondence: al2856@cumc.columbia.edu

<http://dx.doi.org/10.1016/j.neuron.2016.02.019>

SUMMARY

Adult-born granule cells (abGCs) have been implicated in cognition and mood; however, it remains unknown how these cells behave *in vivo*. Here, we have used two-photon calcium imaging to monitor the activity of young abGCs in awake behaving mice. We find that young adult-born neurons fire at a higher rate *in vivo* but paradoxically exhibit less spatial tuning than their mature counterparts. When presented with different contexts, mature granule cells underwent robust remapping of their spatial representations, and the few spatially tuned adult-born cells remapped to a similar degree. We next used optogenetic silencing to confirm the direct involvement of abGCs in context encoding and discrimination, consistent with their proposed role in pattern separation. These results provide the first *in vivo* characterization of abGCs and reveal their participation in the encoding of novel information.

INTRODUCTION

Hippocampal neurogenesis in the adult mammalian brain is a process by which new dentate gyrus (DG) granule cells (GCs) are generated and functionally integrated into hippocampal circuitry (Drew et al., 2013; Toni et al., 2007, 2008; van Praag et al., 2002). In both rodents and humans, a significant fraction of DG neurons are replaced by neurons generated in adulthood (Imayoshi et al., 2008; Spalding et al., 2013). Why this is the case and precisely how young adult-born GCs (abGCs) alter hippocampal circuit function remain open questions.

Behavioral studies have implicated abGCs in memory formation (Zhao et al., 2008); stress and anxiety (Snyder et al., 2011); responses to antidepressant treatments (David et al., 2009; Santarelli et al., 2003); and, most recently, in behaviors requiring contextual discrimination, consistent with a role in pattern separation (Clelland et al., 2009; Kheirbek et al., 2012a; Nakashiba et al., 2012; Sahay et al., 2011a). However, such studies have primarily inferred functions of abGCs from experiments in which adult neurogenesis was chronically ablated or enhanced, i.e., long-term manipulations that may induce compensatory changes (Singer et al., 2011) and/or result in the recruitment of alternative behavioral or cognitive strategies. Furthermore, in these designs abGCs are either absent or more abundant during all phases of testing.

Hypotheses attempting to explain the role of abGCs range from modulating the activity of mature GCs (mGCs) through interactions with local interneurons, to themselves providing the DG's principal output signals (Piatti et al., 2013; Sahay et al., 2011b). Brain slice preparations have provided additional insight into the possible mechanisms by which they may uniquely influence circuit function (Dieni et al., 2013; Marín-Burgin et al., 2012; Temprana et al., 2015; van Praag et al., 2002). For example, adult-born neurons undergo a period of heightened synaptic plasticity 4–6 weeks postmitosis, a critical period during which they have been proposed to have a distinct contribution to behavior (Denny et al., 2012; Ge et al., 2007; Kheirbek et al., 2012b; Schmidt-Hieber et al., 2004). Further observed differences in excitability and plasticity could allow abGCs to encode and transfer information differently than mGCs (Ge et al., 2007; Gu et al., 2012; Schmidt-Hieber et al., 2004; van Praag et al., 2002). However, at present there are no data from the intact brain directly comparing the firing patterns of these subpopulations during behavior. This is because *in vivo* identification of mGCs and abGCs with electrophysiological approaches remains technically challenging (Jung and McNaughton, 1993; Leutgeb et al.,

2007; Neunuebel and Knierim, 2012; Pernía-Andrade and Jonas, 2014). Studies using immediate early gene expression as a proxy for neuronal activation have not identified significant differences in the recruitment of mGCs and abGCs (Stone et al., 2011) during contextual encoding, but this methodology fails to capture the dynamic nature of neuronal encoding.

Here, we have recorded the activity of abGCs *in vivo*, providing the first functional characterization of identified abGCs. Although these cells are more active than mGCs *in vivo*, they are less spatially tuned. Furthermore, we found that mGCs robustly discriminated contexts on the basis of their spatial tuning, while the small population of spatially tuned abGCs seemed to discriminate contexts to a similar or lesser degree, depending on the inclusion criteria and remapping metric applied. We confirmed this online participation of abGCs to the encoding of novel information by transiently suppressing abGCs's activity in distinct epochs of conditioning paradigms, where we showed their essential role in behavioral pattern separation. These experiments extend our understanding of the unique contribution of abGCs to behavior and provide the first characterization of their activity *in vivo*.

RESULTS

Two-Photon Calcium Imaging of DG GCs *In Vivo*

To gain insight into how abGCs behave *in vivo*, we sought to directly observe their activity in the intact brain in response to the manipulation of spatial and contextual cues. This was achieved by performing calcium imaging of the DG in head-restrained mice as they explored a linear virtual environment (Kaifosh et al., 2013; Lovett-Barron et al., 2014) (Figure 1A). Use of this method allowed us to image the activity of abGCs and mGCs simultaneously, which is not yet technically feasible in freely moving mice. To label abGCs, NestinCreER^{T2} mice (Dranovsky et al., 2011) were crossed with a conditional tdTomato reporter line (*Nestin*^{tdTomato}) and pulsed with tamoxifen (TMX) 6 weeks prior to imaging. This led to labeling of 89.5% ± 3.8% of the DCX population of immature cells 6 weeks after induction, indicating ~10% of abGCs were not labeled and thus were not characterized as abGCs. Mice were stereotactically injected in the dorsal DG with a virus expressing GCaMP6f in all GCs. Implantation of a chronic imaging window over the dorsal DG provided the optical access necessary for cell-type-specific imaging of the DG GC layer (Figures 1A and S1, available online). This preparation did not impair hippocampal-dependent contextual conditioning, nor did it impact the overall level of activity in the DG. In addition, window implantation did not impact total number of tdTomato+ abGCs, their dendritic morphology, or the number of proliferating cells in the implanted hemisphere.

In total, we imaged 7,950 mGCs (tdTomato negative) and 446 abGCs (tdTomato positive) from 11 fields of view (FOVs) across 6 mice (Figure S1). The same FOV (Figure S2) was imaged over three trials in which the mouse explored two linear virtual contexts. On the first trial, the mouse explored one of the two contexts (A; chosen at random), then for both the second and third trials it explored the second context (B). This paradigm allowed us to compare activity levels, spatial firing patterns, and remapping dynamics in abGCs and mGCs simultaneously.

abGCs Are More Active Than mGCs *In Vivo*

Consistent with electrophysiological studies reporting sparse GC activity (Alme et al., 2010; Leutgeb et al., 2007; Pernía-Andrade and Jonas, 2014; Schmidt-Hieber et al., 2014), detected calcium transients (Figure S2A) were observed at very low rates in both abGCs and mGCs (Figures 1B–1D; Movie S1). The level of activity was dependent on the animal's behavioral state (Leutgeb et al., 2007; Neunuebel and Knierim, 2012), as calcium transients during running were observed at nearly 2-fold higher rate than during nonrunning epochs (Figure S2C). Running-related calcium transients occurred at significantly greater rates in abGCs than in mGCs across all transients (Figures 1B and 1C) as well as across FOVs (Figure 1D). This difference was most pronounced in the FOVs that displayed the highest levels of activity. The increased activity observed *in vivo* is consistent with reports of greater responsiveness to perforant path activation of abGCs *in vitro* (Marín-Burgin et al., 2012). In addition to having a lower overall fraction of silent cells, the abGC population also contained a higher fraction of highly active cells (Figure 1C, inset). Additionally, across FOVs, we did not detect differences between mGCs and abGCs in the amplitude or duration of detected transients suggesting similar activity-induced calcium dynamics in the two populations (Figure S2B).

abGCs Are Less Spatially Tuned Than mGCs

We next assessed the degree to which abGCs and mGCs were spatially tuned (Figure 2). To limit noise in estimates of the spatial tuning metrics, we included only GC recordings with four or more running-related transients during the trial. For each such GC recording, we calculated a tuning vector as the mean of the vectors pointing in the direction of the mouse's position at the time of each transient onset, inversely weighted by the mouse's occupancy of that position (Figures 2A, 2B, and S3). This vector's orientation and length defined the cell's tuning direction and tuning specificity, respectively. The mean spatial tuning specificity was significantly lower for abGCs than for mGCs (Figure 2C). We did not observe significant reward-related or velocity-related activity in our recordings (Figure S4).

To assess the statistical significance of the tuning specificity difference, for each GC we generated a null distribution by randomly shuffling calcium transient onset times and repeatedly recomputing the tuning specificity. This allowed us to calculate the p value as the fraction of this null distribution that exceeded the GC's tuning specificity. The p value distributions for both mGCs and abGCs differed significantly from chance levels, indicating that spatially tuned cells existed within both populations (Figure 2D). However, the p value distribution for mGC populations was lower than that for abGCs (Figure 2D), suggesting that as a population the mGCs demonstrate a higher degree of spatial tuning than abGCs. Across all significance thresholds, a higher fraction of mature neurons would be categorized as spatially tuned than of young neurons. These findings indicate that abGCs differ from mGCs not just in their level of activity but also in the spatial information carried by their activity.

To investigate whether the observed difference in spatial tuning was dependent on the value of our inclusion threshold, we compared the spatial tuning p values of mGCs and abGCs for

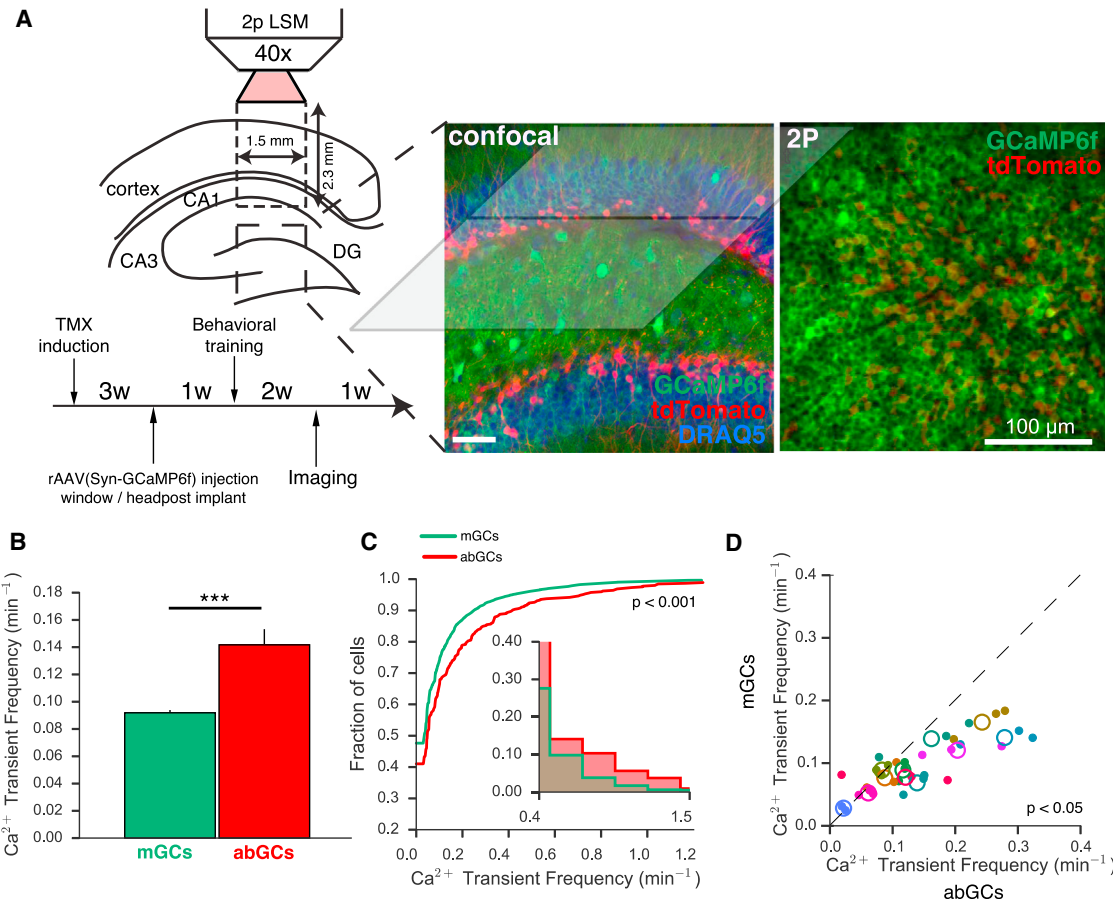


Figure 1. Functional Imaging of abGCs and mGCs

(A) Left: experimental schematic. Two-photon line-scanning microscopy allows for the recording of large populations of GCs in surgically exposed dorsal DG. Experimental timeline as indicated. Middle: confocal image of recovered tissue illustrating the geometry of the preparation. GCs (stained with DRAQ5) express GCaMP6f, with abGCs also expressing tdTomato. Right: time-averaged *in vivo* two-photon image of a representative FOV ($300 \times 300 \mu\text{m}$), containing ~1,000 GCs.

(B) abGCs exhibit a higher rate of running-related calcium transients than mGCs ($p < 0.001$; $n = 7,950$ mGCs, 446 abGCs across 11 FOV in 6 mice; Welch's *t* test, $t_{(8,396)} = -4.14$; each measure is the average of 1–3 recordings for that cell).

(C) Distribution of firing rates across abGCs and mGCs demonstrates significantly different population-level activity ($p < 0.001$; Kolmogorov-Smirnov (KS) test, KS Stat = 0.10).

(D) Scatter of mean abGC and mGC running-related firing rates within each recording session (closed circles) and averaged across sessions for each FOV (open circles). Color reflects FOV as specified in Figure S6. Across imaging fields abGCs were significantly more active than mGCs ($p < 0.05$; $n = 11$ FOV; paired *t* test, $t_{(20)} = 2.88$). The same results were obtained when including all transients (data not shown). Error bars are mean \pm SEM.

different minimum numbers of running-related transients (Figure 2E). At all inclusion thresholds, mean *p* values were lower for mGCs than for abGCs. As expected for a population in which there was no relationship between spatial tuning and activity level, the *p* values for mGCs decreased monotonically with increasing inclusion threshold (statistical power increases, and hence *p* values decrease with greater numbers of transients). The lack of a similar decrease in abGCs suggests a dependence of tuning on activity, whereby the most active abGCs tend to be least tuned (see Figure S3).

It is important to note that a lower tuning specificity could be consistent with an interpretation of multiple place fields, and a difference in this metric could either be attributable to inconsis-

tent tuning or to tuning that is consistent but multipeaked or broader. Estimating the precise number of fields was not possible due to the sparsity of events observed. However, in order to account for the possibility of multipeaked tuning profiles, we also calculated the mutual information between the occupancy-normalized Ca²⁺ transient rate maps and the mouse's position. The traditional definition of spatial information (Skaggs et al., 1993), based on the method of sieves, is a highly biased estimator in the setting of sparse firing rates, as were observed in our data (Paninski, 2003), therefore it was not possible to quantify absolute spatial information rates in these cells. However, a *p* value analysis derived similarly to that of tuning specificity above is immune to this bias, since both the calculated and

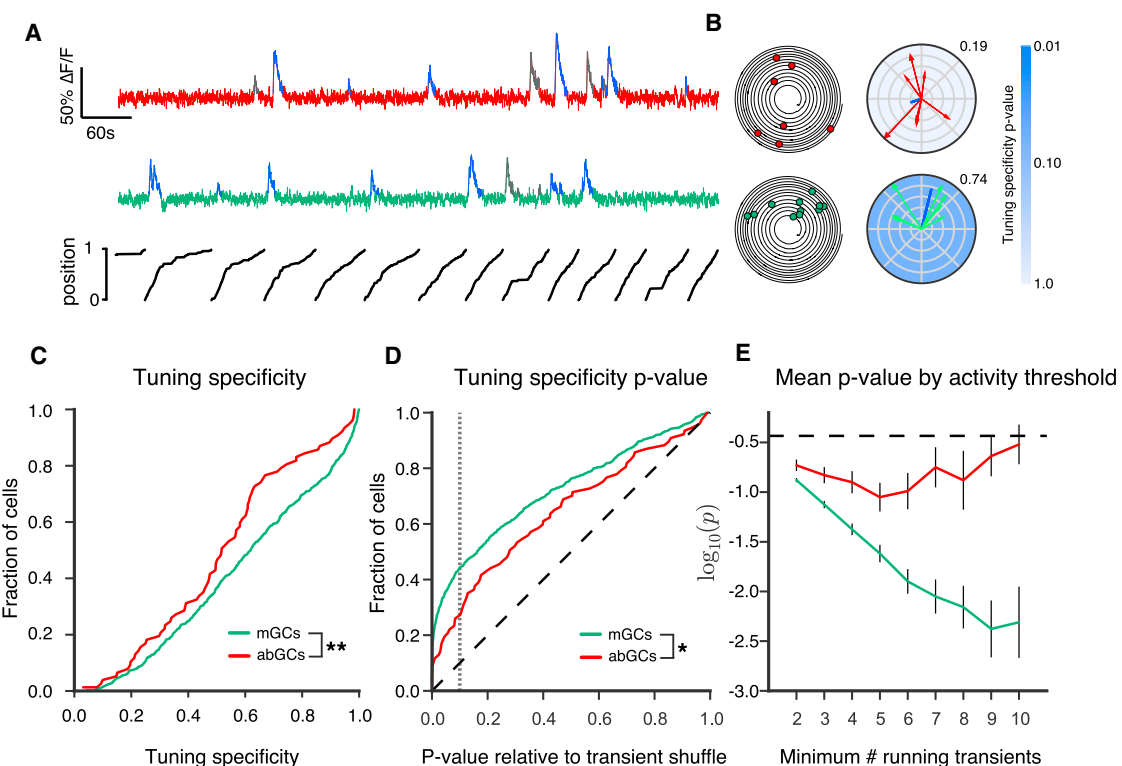


Figure 2. Spatial Tuning of abGCs and mGCs

(A) Time series of calcium signals from an example abGC (red) and mGC (green), with position of the mouse along the circular treadmill belt plotted below. Running-related calcium transients are indicated in blue (all others in gray).

(B) Left: trajectory plot of position (angular coordinate) and time (radial coordinate) with running-related calcium transients as dots along the trajectory. Right: spatial tuning plots for example mGC (green) and abGC (red). Vectors indicate the animal's position at the time of each running-related transient onset, with magnitude determined by the inverse of the fraction of time spent at that position. Blue lines indicate the calculated tuning vectors, whose orientation and magnitude correspond to the tuning direction and specificity, respectively. Tuning specificity is given next to each plot. Tuning specificity p value is indicated by blue shading.

(C) Cumulative distributions of tuning specificity values for active mGCs and abGCs (\geq four running-related transients). The abGC distribution was significantly left shifted as compared to the mGC distribution with few sharply tuned cells ($p < 0.01$; $n = 639$ mGCs, 77 abGCs from 11 FOVs in 6 mice; two-sample KS Test, KS Stat = 0.217, $p < 0.01$).

(D) Cumulative distributions of tuning specificity p values. The p value distributions for mGCs and abGCs differed significantly from each other ($p < 0.05$; KS test, KS Stat = 0.18) and from the uniform distribution (diagonal dashed line) expected in the case of a nonspatially tuned population ($p < 0.001$ for both mGCs and abGCs; KS test, abGCs, KS Stat = 0.25, mGCs KS Stat = 0.35). Gray dashed line indicates $p = 0.1$.

(E) Mean logarithm of the p value for mGCs and abGCs with differing inclusion thresholds for the number of running-related calcium transients. For mGCs, the p values monotonically decrease with increasing inclusion threshold, consistent with the increased statistical power provided by a greater numbers of transients. The lack of such a decrease in the adult-born population suggests that the more active abGCs tend to be less tuned or consist of a mixed population of tuned and untuned cells. The dashed black line shows the expected value for an untuned population.

Error bars are mean \pm SEM.

shuffled distributions are calculated in the same manner (see **Experimental Procedures**). This analysis, which is independent of the tuning specificity metric and does not inherently select for singly peaked tuning profiles, confirmed our primary results. Spatial information p values and tuning specificity p values were linearly related on a logarithmic scale, yielding largely overlapping populations of cells (Figures 4A and 4B). The spatial information p value distributions for both populations differed significantly from chance levels, but the mGC p value distribution was significantly lower than that of abGCs, again suggesting that as a population abGCs are relatively less spatially tuned (Figure 4C). We also observed a similar relationship between the minimum number of transients and the mean spatial information

p value as was described in the tuning specificity analysis (Figure 4D). We saw no consistent evidence of multipeaked firing in the tuning profiles of recordings that satisfied the spatial information, but not the tuning specificity criterion. In summary, this spatial information-based analysis further supports our finding that as a population, abGCs are less sharply tuned than the mGC population.

Contextual Discrimination by abGCs and mGCs

We next assessed the context specificity of spatial representations within the population of spatially tuned mGCs and abGCs (Figure 3). We compared the similarity of GCs' spatial tuning between two sequential exposures to either similar ("A-B") or

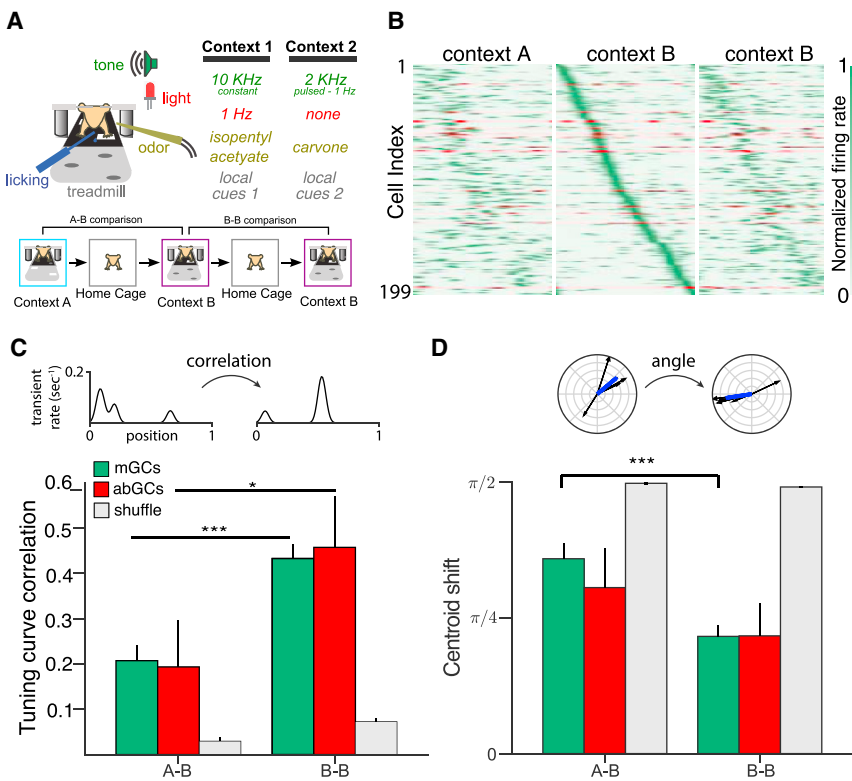


Figure 3. Contextual Coding by abGCs and mGCs

(A) Experimental schematic. Mice ran for three 12 min sessions in contexts A, B, and B (1 hr between runs). A and B refer to either context 1 or 2 (chosen randomly for each experiment).

(B) Remapping of spatial rate maps across sequential context exposures. Smoothed calcium transient rates, normalized to peak for each cell, are plotted as a function of position during three contextual exposures (A, B, B). Cells (mGCs, green; abGCs, red) are ordered according to the position of peak activity during the first exposure to context B. Data is shown for GCs with sufficient tuning specificity and activity ($p < 0.1$, at least four transients) in at least one experiment.

(C and D) Context specificity of spatial representations. Tuning curve correlations of 1D rate maps (C) and centroid shifts (angle between tuning directions) (D) between sequential exposures to different (A-B) or the same (B-B) contexts for all cells shown in (B) (A-B: n = 180 mGCs, 14 abGCs; B-B: n = 174 mGCs, 9 abGCs). The rate map correlations of both populations were more similar in the B-B condition than in A-B (Mann-Whitney U, mGCs: $U_{(150)} = 5,291$, $p < 0.001$; abGCs: $U_{(18)} = 23.0$, $p < 0.05$). In mGCs the tuning shift was larger in the A-B condition than in B-B, although this did not reach significance in abGCs (mGCs: $U_{(150)} = 5,714$, $p < 0.001$; abGCs: $U_{(18)} = 40.0$, $p = 0.34$). In both conditions, the similarity of spatial representations exceeded chance levels as estimated by shuffling cell identity (gray). Error bars are mean \pm SEM.

identical (“B-B”) contexts. The similar contexts A and B shared the same treadmill belt but had different olfactory, auditory, visual, and tactile cues (Figure 3A). We focused our analysis on cells with significant and well-estimated spatial tuning (at least four running-related transients in both sessions and tuning specificity p value below 0.1 in at least one session; Figure 3B). Spatially tuned mGCs displayed a higher correlation of their tuning curves (Figures 3C, S5A, and S5B) and a smaller centroid shift (angle between tuning directions; Figures 3D, S5A, and S5B) in the B-B condition than in the A-B condition. The small number of spatially tuned abGCs satisfying the inclusion criteria displayed a significantly higher correlation of tuning curves in the B-B condition than in A-B, but this result did not hold for the centroid shift metric. When basing the inclusion criteria on the spatial information p value, rather than on the tuning specificity, we similarly observed that mGCs remapped to a greater degree in the A-B than the B-B conditions as assessed by both metrics (Figures 4E and 4F). abGCs did not demonstrate a significant difference in remapping in the A-B versus B-B comparison, though it is important to note that this was difficult to assess given the low number of abGCs meeting the inclusion threshold. While the A-B-B paradigm allowed us to measure reorganization in response to the manipulation of a novel context, B-B-A and other related paradigms will allow for assessment of reorganization in a more familiar environment.

We next investigated whether DG GCs can discriminate between similar contexts solely on the basis of their activity level

throughout the exposure to these contexts, which would be indicative of rate remapping (Figures 5, S5C, and S5D). To determine this, we computed population vectors (Figure 5A) whose components were the time-averaged calcium transient rate (Figure 5B) or the transient AUC rate (Figure 5C) for each cell during the trial. By measuring the angle between population vectors (Θ_{B-B} , Θ_{A-B}) we found that for both mGCs and abGCs the population vectors were as closely aligned between sequential exposures to the same (B-B) versus different (A-B) contexts. To control for the disparities in sample size between adult-born and mature populations, we studied the pseudopopulation vectors (Figure 5D) obtained by pooling GCs across all FOVs. The contextual specificity ($\Theta_{B-B} - \Theta_{A-B}$) for the abGC pseudopopulation fell well within the distribution obtained from random subsamplings of the mGC pseudopopulations for both the transient rate (Figure 5E) and transient AUC rate (Figure 5F) vectors. This indicates that in our experimental paradigm, both abGCs and mGCs discriminate between contexts at the level of their spatial tuning rather than through spatially independent changes in firing rate.

abGCs Actively Participate in the Encoding of Novel Information

Finally, we asked whether abGCs are required for encoding a novel environment. In order to address this question, we expressed *archaerhodopsin* (*Arch*) in abGCs by crossing the

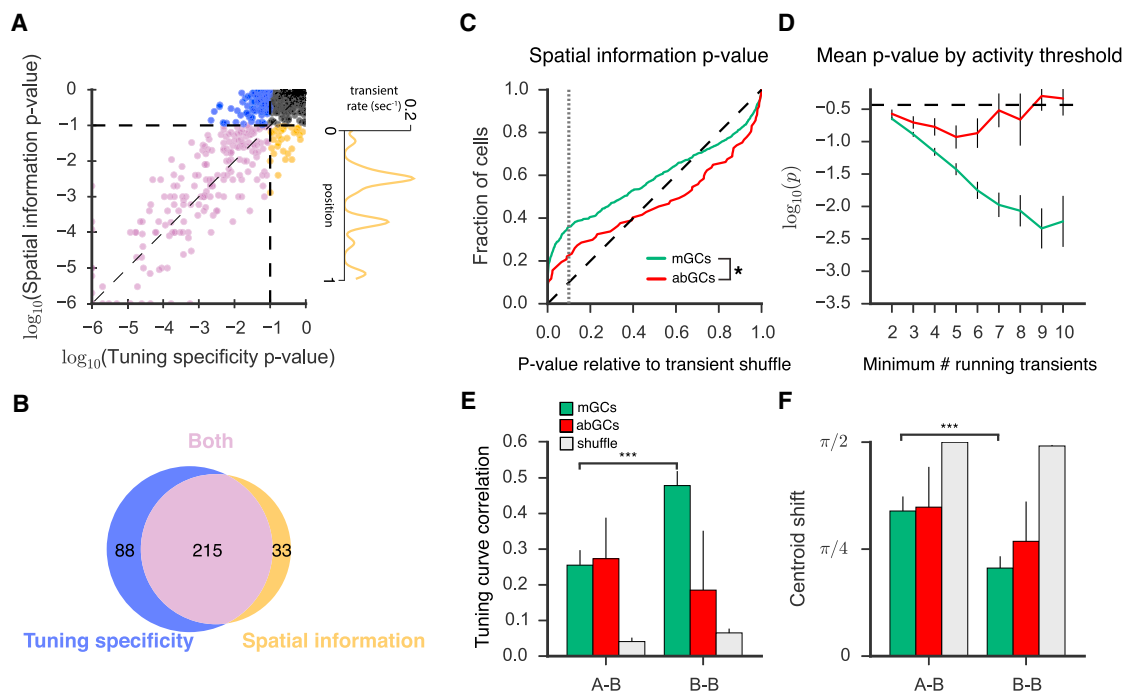


Figure 4. Spatial Information in abGCs

(A) For each cell firing at least four running-related transients, we calculated the spatial information p value and tuning specificity p value by shuffling the events in time and repeatedly recalculating either corresponding metric. Values are highly correlated on a log scale ($r = 0.91$, Pearson's R). Cells are colored according to whether they met the tuning specificity p value inclusion criterion only (blue), the spatial information p value criterion only (gold), both (purple), and neither (black). Right panel: the tuning profile of a cell meeting the spatial information, but not the tuning specificity, criteria is shown.

(B) Venn diagram demonstrates overlap in populations meeting the two inclusion criteria ($p < 0.10$).

(C) Cumulative distributions of spatial information p values. The p value distributions for mGCs and abGCs differed significantly from each other (KS test, KS Stat = 0.17, $p < 0.05$) and from the uniform distribution (diagonal dashed line) expected in the case of a nonspatially tuned population (KS test; mGCs: KS Stat = 0.26, $p < 0.001$; abGCs: KS Stat = 0.146, $p < 0.05$). Gray dashed line indicates $p = 0.1$.

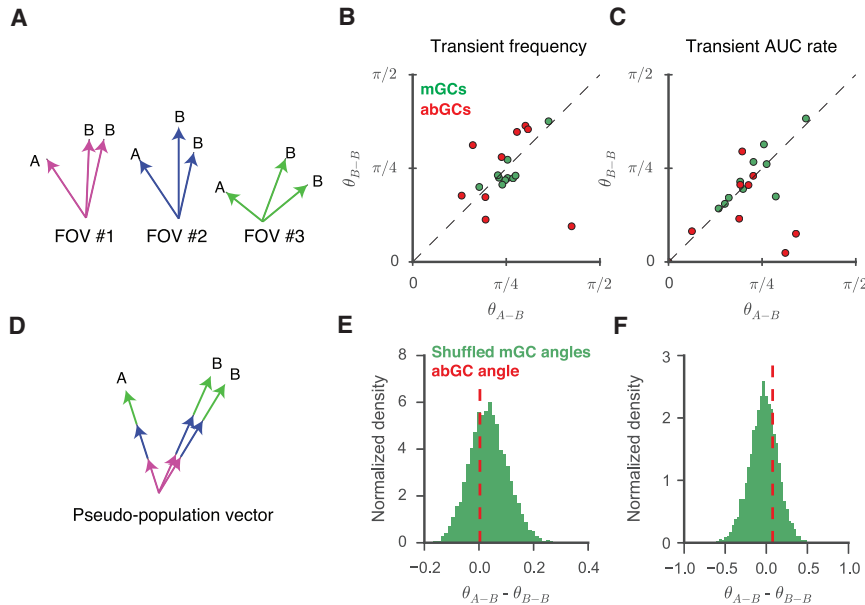
(D) Mean logarithm of the p value for mGCs and abGCs with differing inclusion thresholds for the number of running-related calcium transients. A similar relationship is seen as described in Figure 2E.

(E and F) Contextual discrimination analysis with inclusion criteria based on spatial information p value. For mGCs (A-B, $n = 100$; B-B, $n = 106$) the tuning curve correlation (E; Mann-Whitney U, $U_{(204)} = 3,597$, $p < 0.001$) and centroid shift (F; Mann-Whitney U, $U_{(204)} = 3,798$, $p < 0.001$) were both significantly more similar in the B-B condition than in A-B. This relationship was not observed (Mann-Whitney U; E; $U_{(14)} = 26.0$, $p = 0.45$; F; $U_{(14)} = 23.0$, $p = 0.32$) in the few abGCs (A-B, $n = 11$; B-B, $n = 5$) meeting the spatial information inclusion criterion.

Error bars are mean \pm SEM.

NestinCreER^{T2} mouse line with conditional Arch-eGFP mice (Madisen et al., 2012) (*Nestin^{Arch}*; Figure 6A). *Nestin^{Arch}* mice given TMX in adulthood expressed the transgene in ~80%–90% of abGCs in the DG (Figure S6). Targeted fiber optic implantation allowed local light delivery and thus control of 6-week-old and younger DG abGCs expressing Arch during behavior (Figure 6A). To examine effects on context encoding, mice received local illumination of the dorsal DG as they explored a conditioning context before receiving a single foot shock; they were then exposed to this same context 24 hr later in the absence of light. *Nestin^{Arch}* mice froze significantly less than control mice, indicating that activity in abGCs was required for effective contextual encoding (Figure 6B). Optical stimulation of abGCs impaired conditioning, presumably by disrupting the circuit (Figure S6). Optical modulation of abGCs did not impact shock reactivity, anxiety-related behavior, or general locomotor activity (Table S1).

We next tested whether transient inhibition of abGCs impacts behavioral pattern separation, the ability to discriminate between similar contexts, which has been proposed to require abGCs (Clelland et al., 2009; Kheirbek et al., 2012a; Nakashiba et al., 2012; Sahay et al., 2011a). We suppressed abGC activity either during exposure to the conditioning context A or to the similar, nonconditioned context B (Figures 6C and 6D). While silencing abGCs during exposure to the conditioning context did not impair the development of a discriminatory response (Figure 6C), silencing these cells during exposure to the similar context resulted in impaired discrimination (Figure 6D), indicating that activity of the abGCs is required for behavioral pattern separation specifically during exposure to the ambiguous context. *Nestin^{Arch}* mice could discriminate between very distinct contexts and between similar contexts when silencing was performed after the mice had already learned to discriminate (Figure S6). Together, these data extend our understanding of the role played by abGCs during pattern separation on a behavioral level.



(E and F) Lack of evidence for activity-based discrimination ($\theta_{A-B} - \theta_{B-B}$) for either transient frequency (E) and transient AUC rate (F). The dotted red line indicates the difference in the angles between the abGC pseudopopulation vectors. The difference was consistent with the distribution (green histogram) of such differences attained by repeatedly randomly downsampling similarly constructed pseudopopulations of mature cells (E, percentile = 34; F, percentile = 73; see Experimental Procedures).

DISCUSSION

The results presented herein expand our understanding of the contribution of abGCs to the function of the DG. We found that activity was sparse in both the mGC and abGC populations, consistent with *in vivo* extracellular electrophysiological studies and intracellular recordings (Alme et al., 2010; Leutgeb et al., 2007; Pernía-Andrade and Jonas, 2014; Schmidt-Hieber et al., 2014). By monitoring for the first time *in vivo* the activity of this population of cells while mice explored multisensory contexts, we reveal that GCs 6 weeks and younger fire at a higher rate *in vivo* than the mature population, complementing recent findings showing that young GCs are more excitable in *in vitro* preparations (Marín-Burgin et al., 2012). In the absence of combined electrophysiological recordings, we cannot eliminate the possibility that transient differences in Ca^{2+} buffering might affect our activity estimates (Brandt et al., 2003), though we detected no consistent differences in the amplitude or duration of detected somatic Ca^{2+} transients (see also Marín-Burgin et al., 2012) at the FOV or individual mouse level.

We further found that abGCs were less spatially tuned than mGCs. The lower tuning specificity we observed could either be attributable to less stable spatial firing patterns or to the presence of stable but multipeaked tuning profiles, as might be expected from recent electrophysiological recordings describing broader, multipeaked tuning profiles at the hilar-GCL border, where most abGCs reside (Alme et al., 2010; Neunuebel and Knierim, 2012). In addition to a lower tuning specificity, however, we found that abGCs fire with relatively less spatial information. Although our behavioral paradigm did not allow for the systematic study of time coding (Kraus et al., 2013; MacDonald et al.,

Figure 5. Mean Activity in GCs Does Not Code for Context

(A) Schematic of population vector analysis. Activity-based vectors were defined for each experiment, and angles were measured between sequential exposures to the same (θ_{B-B}) or similar (θ_{A-B}) contexts.

(B and C) Scatter of population vector angles across the two conditions in which vector components are defined as transient frequency (B) or rate of transient AUC (area under the curve of significant Ca^{2+} transients divided by the total time) (C). Each point corresponds to mature (green) or newborn (red) cells from one FOV. For neither abGC (B; paired t test, $T_{(16)} = 0.04$, $p = 0.97$; C; $T_{(16)} = 1.25$, $p = 0.25$) nor mGC (B; $T_{(18)} = 1.53$, $p = 0.16$; C; $T_{(18)} = -0.32$, $p = 0.76$) populations were the vectors more similar for sequential exposures to the same context than for sequential exposures to different contexts.

(D) For each contextual exposure, we calculated a single pseudopopulation vector by concatenating the newborn population vectors from all FOVs. Schematic is drawn to illustrate the case of activity-based discrimination.

2011) in the GC population, we did not find that GC activity was related to other dimensions of the task, such as reward or velocity (Kropff et al., 2015).

Our results also suggested the existence of a relationship between activity and tuning in abGCs, in which the highly active abGCs are less spatially tuned. These results may be related to the maturational heterogeneity of the labeled cells and are consistent with a model in which young abGCs are initially more active and less spatially tuned but within 6 weeks become more similar to the less active and more spatially tuned mature cells. It is important to note that the *Nestin* *tdTomato* labeling system does not provide an exact birthdate of the recorded neurons but rather results in the cumulative labeling of abGCs 6 weeks and younger. Consequently, we are unable to unequivocally distinguish abGCs between 0 and 6 weeks in our recordings. The recorded abGCs exhibited strong state-dependent modulation (Figure S2C), presumably driven by their glutamatergic innervation and local integration into the DG circuit. As both of these developmental events have been demonstrated to occur after approximately 3 weeks of development (Espósito et al., 2005; Ge et al., 2006, 2007; Toni et al., 2007), this suggests that our functional characterization was based predominantly on cells in the 3–6 week age range. Future studies incorporating the imaging techniques described here with retroviral approaches for labeling age-matched cohorts of abGCs will allow for a more detailed determination of the developmental timeline of abGC properties *in vivo*. Such future studies will allow us to track (in the 3–6 week range) the transition from an immature to a mature functional phenotype.

Our *in vivo* imaging data suggest that the small population of spatially tuned abGCs differentiated novel contexts on the basis

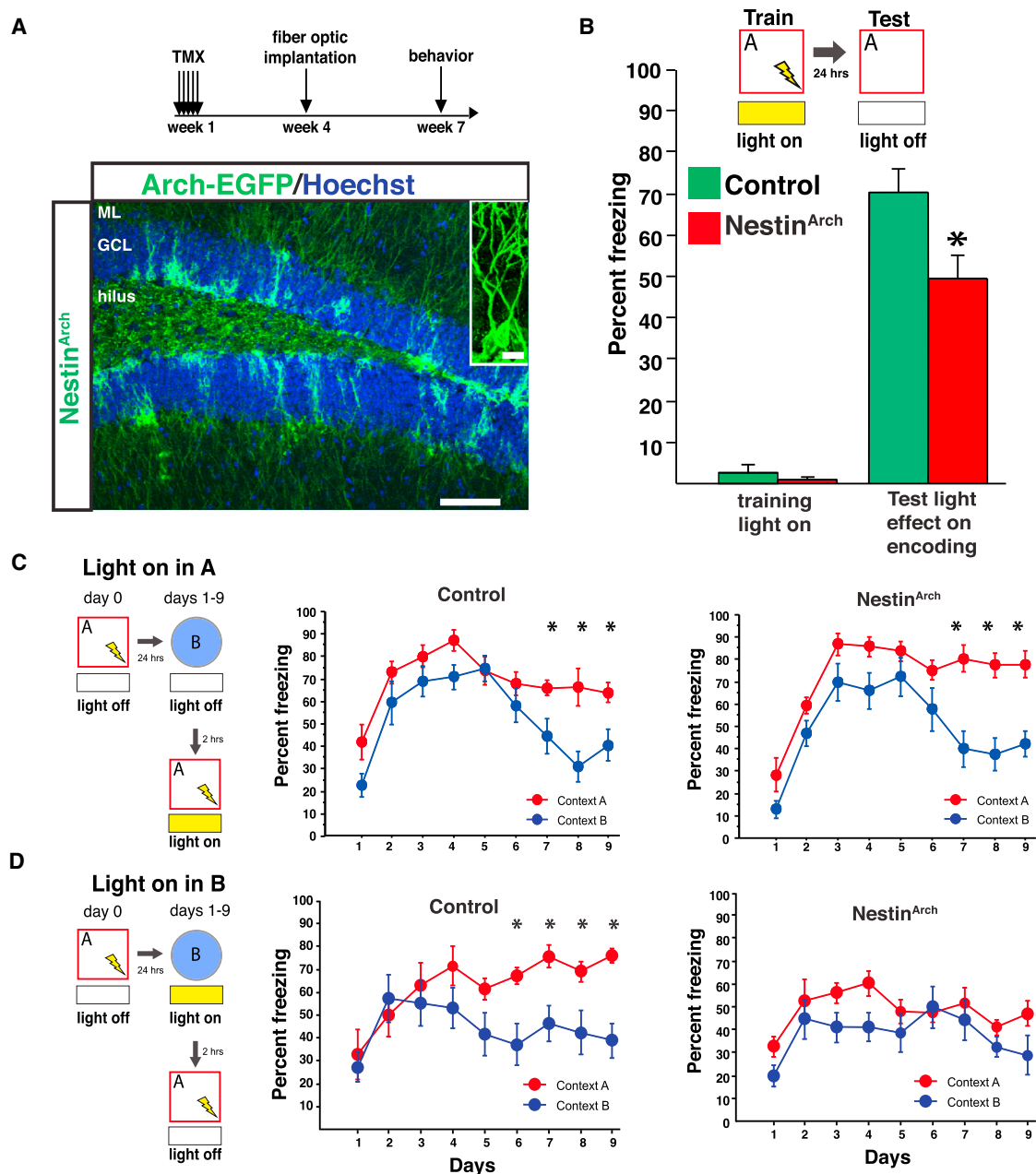


Figure 6. abGCs Participate in Memory Encoding and Discrimination

(A) Experimental design. Right: expression of Arch in abGCs (Scale bar, 100 μ m; inset, 10 μ m).

(B) Yellow-light inhibition of dorsal abGCs during training impaired encoding of contextual fear ($n = 8$ control, 9 Nestin^{Arch}; group effect $F_{(1,15)} = 6.3$, $p = 0.02$; groupXtraining interaction $F_{(1,15)} = 5.4$, $p = 0.03$; on test day $t_{15} = -2.5$, $p = 0.02$).

(C and D) Acute inhibition of abGCs impairs behavioral pattern separation. (C) Mice discriminated when abGCs were inhibited in the conditioning context ($n = 7$ control, 8 Nestin^{Arch}; groupXdayXcontext interaction $F_{(8,208)} = 0.581$, $p = 0.79$. Control: context effect $F_{(1,12)} = 7.243$, $p = 0.02$; dayXcontext interaction $F_{(8,96)} = 2.094$, $p = 0.0436$. Nestin^{Arch}: context effect $F_{(1,14)} = 10.631$, $p = 0.006$; dayXcontext effect $F_{(8,112)} = 3.706$, $p = 0.007$). (D) Mice did not discriminate when abGCs were inhibited in the unconditioned context ($n = 8$ control, 7 Nestin^{Arch}; groupXdayXcontext interaction $F_{(8,208)} = 1.9$, $p = 0.04$. Control: context effect $F_{(1,13)} = 4.8$, $p = 0.04$; dayXcontext interaction $F_{(8,104)} = 3.1$, $p = 0.004$. Nestin^{Arch}: context effect $F_{(1,12)} = 4.1$, $p = 0.06$; dayXcontext effect $F_{(8,96)} = 0.6$, $p = 0.74$). Error bars are mean \pm SEM.

of their spatial tuning to a similar and possibly weaker degree than mGCs, depending on the metric and inclusion criteria applied. This, combined with the fact that we observed so few

well-tuned abGCs in spite of our large number of recordings, suggests that the unique role of abGCs in contextual discrimination behaviors may not be attributable to the spatial distribution

of their firing or the remapping of their fields. The broader tuning profile of abGCs (compared to mGCs) is consistent with computational models of GC dynamics and might support the encoding of novel features in the environment (Aimone et al., 2011; Temprana et al., 2015). This would also be consistent with our finding that silencing these neurons during exposure to the novel context (but not the familiar one) prevents contextual discrimination learning. Alternatively, the abGC population may modulate local excitatory/inhibitory tone in the DG and CA3 (Gu et al., 2012; Restivo et al., 2015; Toni et al., 2008) and could consequently shape spatial and contextual representations. There is indeed evidence from ablation studies that abGCs may modulate the activity of mGCs, possibly via their influence on the DG microcircuit (Burghardt et al., 2012; Drew et al., 2015; Ikrar et al., 2013; Lacefield et al., 2012; Park et al., 2015). Future studies should test this hypothesis directly by using the methods described here to assess changes in mGC spatial and contextual representations following inhibition of abGCs.

In addition, we find that transient inhibition of abGCs impairs behavior, specifically contextual encoding and discrimination, consistent with a proposed role in behavioral pattern separation (Clelland et al., 2009; Kheirbek et al., 2012a, 2012b; Nakashiba et al., 2012; Sahay et al., 2011a). These studies complement recent optogenetic studies describing a role for DG GCs in memory processes (Denny et al., 2014; Gu et al., 2012; Kheirbek et al., 2013). Furthermore, we demonstrate that in a pattern separation task, activity of the abGCs is required during exposure to the novel ambiguous context, but not during exposure to the conditioning context. This is likely due to a deficit in contextual encoding, due to an inability in *Nestin^{Arch}* mice to encode context B as the safe context. This is in agreement with our results in one-trial contextual fear conditioning, where silencing abGCs during the first exposure to context A impaired the ability to encode this context. In the pattern separation experiment, when abGC silencing takes place in context A, freezing keeps increasing because learning is reinforced each day by a foot shock. In contrast, when silencing takes place in context B, freezing decreases in both contexts. This suggests that in these conditions, mice were confused when exposed to both contexts A and B and could no longer encode them as safe or fearful nor discriminate between them.

It is important to note that in this study, the behavior measured during optical inhibition of abGCs in contextual fear discrimination tasks differed from that in the head-fixed preparation during imaging. It was not possible for us to perform our behavioral and imaging experiments in identical conditions, as animals are known to freeze in response to an unconditioned stimulus in our head-fixed paradigm, and thus we cannot measure spatial tuning and remapping in a fear-conditioned animal. Future experiments combining freely moving *in vivo* imaging designs (Ziv et al., 2013) with behavioral pattern separation tasks will allow for analysis of changes in abGC response profiles to novel or conditioned contexts.

Our experimental preparation required a partial lesion of ipsilateral area CA1 in order to obtain high-resolution optical access to the DG. While DG-mediated behavior was normal in the experimental animals (Figures S1D and S1E), we cannot rule out the possibility that chronic circuit reorganization or the implementa-

tion of an alternate circuit strategy might occur in this preparation. Although the implant did not impact overall levels of neurogenesis, or the morphological features of recorded abGCs, we cannot exclude the possibility that the properties of abGCs and mGCs may be differentially affected by the surgical preparation, due, for example, to the potential disruption of grid cell activity in the medial entorhinal cortex (Bonnevie et al., 2013). In the future, less-invasive techniques should complement the results of this study.

Our data not only demonstrate the importance of abGCs for encoding and disambiguating contextual information but also provide insights into the circuit dynamics underlying these processes. Impairments in pattern separation have been proposed to contribute to the excessive generalization of memory often seen in anxiety and depression as well as in age-related disorders such as mild cognitive impairment (Kheirbek et al., 2012a; Leal et al., 2014; Yassa et al., 2011). A mechanistic understanding of how abGCs contribute to hippocampus-dependent memory processing will provide insights not only into the normal function of adult hippocampal neurogenesis but also into the therapeutic potential of this unique form of plasticity.

EXPERIMENTAL PROCEDURES

Full details of the experimental procedures are provided in the [Supplemental Information](#).

Mice, Viruses, and Stereotactic Surgery

All experiments were conducted in accordance with the U.S. NIH guidelines and with the approval of the Columbia University and New York State Psychiatric Institute Institutional Animal Care and Use Committees. Male *Ai9*, *Ai35*, *Nestin-CreER^{T2}*, and controls were generated as previously described (Dranovsky et al., 2011; Madisen et al., 2010, 2012). For imaging experiments, recombinant adeno-associated viruses carrying the GCaMP6f gene were obtained from the Penn Vector Core (AAV1.Syn.GCaMP6f.WPRE.SV40) with titer of $2\text{--}4 \times 10^{13}$. The dorsal DG of male mice (8 weeks of age) was stereotactically injected at -1.5 mm AP; -2.3 mm ML; and -1.8 , -1.65 , -1.5 mm DV relative to the cortical surface. Mice were then surgically implanted with an imaging window over the left dorsal DG and implanted with a stainless-steel headpost for head fixation during imaging experiments (see [Supplemental Information](#)). For optogenetic experiments, male mice (8 weeks of age) were surgically implanted with fiber optics targeted to the dorsal DG (± 1 mm ML, -1.5 mm AP, -1.7 mm DV) using published protocols (Kheirbek et al., 2013).

In Vivo Two-Photon Imaging

We used the same imaging system as described previously (Kaifosh et al., 2013; Lovett-Barron et al., 2014), with the addition of an 8 kHz resonant galvanometer (Bruker). All images were acquired with a Nikon 40 \times NIR water-immersion objective (0.8 NA, 3.5 mm WD) in distilled water. We continuously acquired red (tdTomato) and green (GCaMP6f) channels separated by an emission cube set (green, HQ525/70 m-2p; red, HQ607/45 m-2p; 575dcxr, Chroma Technology) at 1024 \times 1024 pixels covering 300 $\mu\text{m} \times$ 300 μm at 15 Hz with photomultiplier tubes (green GCaMP fluorescence, GaAsP PMT, Hamamatsu Model 7422P-40; red tdTomato fluorescence, multialkali PMT, Hamamatsu R3896). A custom dual stage preamp (1.4×10^5 dB, Bruker) was used to amplify signals prior to digitization.

For training, mice were water restricted (>90% predeprivation weight) and trained to run on a cue-deplete burlap treadmill belt for water reward over the course of 1–2 weeks. We applied a progressively restrictive water reward schedule, with mice initially receiving 40 randomly placed rewards per lap and ultimately receiving 3 randomly placed rewards per lap. Mice were habituated to the optical instrumentation, then trained for 20 min daily until they regularly ran at least one lap per minute. For contexts, similar to our previous work, each

context (1 and 2) consisted of the same treadmill belt (the same sequence of three joined fabric ribbons) but was distinct in its visual, auditory, tactile, and olfactory stimuli (Figure 4A) (Lovett-Barron et al., 2014). During imaging sessions, mice received three randomly placed water rewards per lap, with reward positions changing randomly each lap. To allow for comparison of GC activity between similar contexts, the same three fabrics were used in the same order, but the locations of all of the tactile cues were shuffled between the two belts.

Imaging Analysis

Processing of Ca^{2+} Fluorescence Data

All imaging data were analyzed using the SIMA software package (Kaifosh et al., 2014). Motion correction was performed using a 2D Hidden Markov Model (Dombeck et al., 2007; Kaifosh et al., 2013), with modifications to accommodate the specific features of data acquired with resonant galvanometers. Only the green GCaMP channel was used for estimating motion artifacts. In cases where motion artifacts were not adequately corrected, the affected data were discarded from further analysis. The especially sparse activity of dentate GCs prevented the successful application of activity-based segmentation methods. Therefore, we used the SIMA project's ROI Buddy graphical user interface (Kaifosh et al., 2014) to draw regions of interest (ROIs) over GC somata visible in the time-averaged image of the motion-corrected green/GCaMP6f channel. We also used this software to determine the correspondence of ROIs across datasets from different trials in which the same FOV was imaged. To prevent the introduction of any bias, the red tdTomato channel was not viewed when drawing ROIs but only referenced after all ROIs had been drawn in order to tag ROIs over tdTomato-expressing cells as newborn GCs.

Dynamic GCaMP6f fluorescence signals were extracted from ROIs using SIMA according to the previously described formulation (Kaifosh et al., 2014). We then computed the relative fluorescence changes ($\Delta F/F$) (as described in Jia et al., 2011), with uniform smoothing window $t_1 = 3$ s and baseline size $t_2 = 60$ s. We detected statistically significant calcium transients as described previously (Dombeck et al., 2007; Lovett-Barron et al., 2014). In order to improve our sensitivity, we then recalculated the baseline of the raw signal after masking frames identified previously as occurring during a significant transient. $\Delta F/F$ was then recalculated and transients re-estimated. Transients less than 1 s were removed to reduce false positives. This iterative procedure was repeated three times and effectively removed the transient contamination from the calculated baseline.

Spatial Tuning Vector and Tuning Specificity p Value Analysis

When evaluating the spatial tuning of GCs, we restricted our analysis to running-related epochs, defined as consecutive frames of forward locomotion (defined as an imaging frame in which at least one forward pair of beam breaks occurred) at least 1 s in duration and with a minimum peak speed of 5 cm/sec. Consecutive epochs separated by <0.5 s were merged. Running-related transients were defined as those that were initiated during a running-related epoch. Transient start was defined as the first imaging frame with mean fluorescence $\geq 2\sigma$, with σ equal to the SD of the baseline frames. Offset was defined as the first frame with mean fluorescence $\leq 0.5\sigma$ (Dombeck et al., 2007). The spatial tuning vector was calculated as $\sum \frac{e^{i\theta_j}}{|\theta_j|}$, where θ_j is the position of the mouse at the onset time of the j^{th} running-related transient, and $e^{i\theta_j}$ is the fraction of running frames acquired at position θ_j . Only the animal's position at the time of transient onset was used for constructing the tuning vector and rate maps (see Remapping Analysis section below), as the calcium decay kinetics are intrinsic to the GCaMP6f indicator and are not sensitive to the animal's running speed (a similar onset-based approach was implemented previously by Ziv et al., 2013). In order to assess the significance of the spatial selectivity, for each cell we generated a null tuning distribution by shuffling the transient onset times (restricted to running frames) and repeatedly recomputing the tuning specificity. This process was repeated 100,000 times, and the p value was defined as the fraction of this distribution that exceeded the GC's tuning specificity.

Spatial Information p Value Analysis

For each cell we first computed the spatial information content (Skaggs et al., 1993) as $I_N = \sum_{i=1}^N \lambda_i \ln \frac{\lambda_i}{\bar{\lambda}} p_i$, where λ_i and p_i are the transient rate and fraction of time spent in the i^{th} bin, $\bar{\lambda}$ is the overall firing rate, and N is the number of bins.

We computed I_N for multiple values of $N = 2, 4, 5, 8, 10, 20, 25$, and 100. We then created 100,000 random reassessments of the transient onset times within the running-related epochs and recomputed the values of \hat{I}_N^s , where s is the index of the shuffle. To roughly correct for biases in the calculation of mutual information, we then subtracted the mean of this null distribution from all estimates to obtain values $\hat{I}_N = I_N - \frac{1}{100,000} \sum_{s=1}^{100,000} \hat{I}_N^s$. Finally, we computed a single estimate of the information content for the true transient onset times, $\hat{I} = \max_N \hat{I}_N$, and for the shuffles, $\hat{I}_s = \max_N \hat{I}_N^s$. The spatial tuning p value was taken as the fraction of values of s for which \hat{I} exceeded \hat{I}_s .

Remapping Analysis

Rate maps were formed by dividing the number of transients starting in each bin by the occupancy of that bin. We calculated rate maps with 100 position bins and smoothed with a Gaussian kernel ($\sigma = 3$ bins). The tuning curve correlation for each cell was defined as the Pearson correlation coefficient between tuning curves for a cell in the two sequential context exposures. The centroid shift for each cell was defined as the angle (in radians) between the tuning directions calculated for the two context exposures. For both metrics, the shuffle distributions were calculated by estimating the tuning curve correlations or tuning shifts when cells were paired by a subsampled Cartesian product of cell identities (1,000 pairs per shuffle).

Behavioral Testing

In Arch experiments, the patch cables were interfaced to an FC/PC rotary joint (Doric lenses), which was attached on the other end to a 593.5 nm laser diode that was controlled by a Master-8 stimulator (AMPI). Fear conditioning took place in Coulbourn Instruments fear conditioning boxes. See *Supplemental Information* for full details of behavioral procedures.

Statistics

For all optogenetic behavioral data, data were analyzed using ANOVA with repeated measurements where appropriate. All tests are described in the appropriate figure legends. Group numbers were based on previous optogenetic and two-photon imaging experiments (Kheirbek et al., 2013; Lovett-Barron et al., 2014). For imaging data, for all normally distributed data, a Welch's two-sample t test was used for comparison of means with $n - 1$ degrees of freedom. The Mann-Whitney U test was used for comparison of means in non-normally distributed data with $n - 1$ degrees of freedom. A paired student's t test was used for comparison of means in paired data with $n - 1$ degrees of freedom. The one-sided Kolmogorov-Smirnov (KS) test was used for testing the hypothesis that a distribution was drawn from an underlying theoretical distribution with $n - 1$ degrees of freedom (uniformity in the case of Figure 2E). The two-sided two-sample KS test with $n - 1$ degrees of freedom was used for testing the null hypothesis that two empirical distributions were drawn from the same continuous underlying distribution.

SUPPLEMENTAL INFORMATION

Supplemental Information includes Supplemental Experimental Procedures, six figures, one table, and one movie and can be found with this article online at <http://dx.doi.org/10.1016/j.neuron.2016.02.019>.

AUTHOR CONTRIBUTIONS

N.B.D., R.H., A.L., and M.A.K. conceived the project, designed the experiments, and wrote the manuscript. N.B.D., P.K., J.D.Z., A.L., and M.A.K. performed experiments and analyzed data. M.L.-B., J.T., C.A.D., E.M.B., A.R.G., and L.J.D. assisted with experiments and provided essential reagents, expertise, and input to the manuscript.

ACKNOWLEDGMENTS

We thank L. Looger, S. Fusi, and A. Fenton for discussion and comments; H. Zeng for Ai32 and Ai35 mice; and the GENIE Program at the Janelia Farm Research Campus for GCaMP6f. N.B.D. is supported by NINDS F30NS090819. P.K. is a Howard Hughes Medical Institute International Predoctoral Fellow. M.L.-B. was supported by a Canadian Natural Sciences

and Engineering Research Council postgraduate scholarship. A.L. is supported by NIMH 1R01MH100631, 1U01NS090583, 1R01NS094668, the Searle Scholars Program, the Human Frontier Science Program, and the McKnight Memory and Cognitive Disorders Award. R.H. is supported by NIH R37 MH068542, NIA R01 AG043688, New York State Stem Cell Science (NYSTEM), and the Hope for Depression Research Foundation. M.A.K. was supported by NIMH K01MH099371, NARSAD, and NYSTEM.

Received: December 4, 2015

Revised: January 29, 2016

Accepted: February 10, 2016

Published: March 10, 2016

REFERENCES

- Aimone, J.B., Deng, W., and Gage, F.H. (2011). Resolving new memories: a critical look at the dentate gyrus, adult neurogenesis, and pattern separation. *Neuron* 70, 589–596.
- Alme, C.B., Buzzetti, R.A., Marrone, D.F., Leutgeb, J.K., Chawla, M.K., Schaner, M.J., Bohanick, J.D., Khoboko, T., Leutgeb, S., Moser, E.I., et al. (2010). Hippocampal granule cells opt for early retirement. *Hippocampus* 20, 1109–1123.
- Bonnevie, T., Dunn, B., Fyhn, M., Hafting, T., Derdikman, D., Kubie, J.L., Roudi, Y., Moser, E.I., and Moser, M.B. (2013). Grid cells require excitatory drive from the hippocampus. *Nat. Neurosci.* 16, 309–317.
- Brandt, M.D., Jessberger, S., Steiner, B., Kronenberg, G., Reuter, K., Bick-Sander, A., von der Behrens, W., and Kempermann, G. (2003). Transient calretinin expression defines early postmitotic step of neuronal differentiation in adult hippocampal neurogenesis of mice. *Mol. Cell. Neurosci.* 24, 603–613.
- Burghardt, N.S., Park, E.H., Hen, R., and Fenton, A.A. (2012). Adult-born hippocampal neurons promote cognitive flexibility in mice. *Hippocampus* 22, 1795–1808.
- Clelland, C.D., Choi, M., Romberg, C., Clemenson, G.D., Jr., Fragniere, A., Tyers, P., Jessberger, S., Saksida, L.M., Barker, R.A., Gage, F.H., and Bussey, T.J. (2009). A functional role for adult hippocampal neurogenesis in spatial pattern separation. *Science* 325, 210–213.
- David, D.J., Samuels, B.A., Rainer, Q., Wang, J.W., Marsteller, D., Mendez, I., Drew, M., Craig, D.A., Guiard, B.P., Guilloux, J.P., et al. (2009). Neurogenesis-dependent and -independent effects of fluoxetine in an animal model of anxiety/depression. *Neuron* 62, 479–493.
- Denny, C.A., Burghardt, N.S., Schachter, D.M., Hen, R., and Drew, M.R. (2012). 4- to 6-week-old adult-born hippocampal neurons influence novelty-evoked exploration and contextual fear conditioning. *Hippocampus* 22, 1188–1201.
- Denny, C.A., Kheirbek, M.A., Alba, E.L., Tanaka, K.F., Brachman, R.A., Laughman, K.B., Tomm, N.K., Turi, G.F., Losonczy, A., and Hen, R. (2014). Hippocampal memory traces are differentially modulated by experience, time, and adult neurogenesis. *Neuron* 83, 189–201.
- Dieni, C.V., Nietz, A.K., Panichi, R., Wadiche, J.I., and Overstreet-Wadiche, L. (2013). Distinct determinants of sparse activation during granule cell maturation. *J. Neurosci.* 33, 19131–19142.
- Dombeck, D.A., Khabbaz, A.N., Collman, F., Adelman, T.L., and Tank, D.W. (2007). Imaging large-scale neural activity with cellular resolution in awake, mobile mice. *Neuron* 56, 43–57.
- Dranovsky, A., Picchini, A.M., Moadel, T., Sisti, A.C., Yamada, A., Kimura, S., Leonardo, E.D., and Hen, R. (2011). Experience dictates stem cell fate in the adult hippocampus. *Neuron* 70, 908–923.
- Drew, L.J., Fusi, S., and Hen, R. (2013). Adult neurogenesis in the mammalian hippocampus: why the dentate gyrus? *Learn. Mem.* 20, 710–729.
- Drew, L.J., Kheirbek, M.A., Luna, V.M., Denny, C.A., Cloidt, M.A., Wu, M.V., Jain, S., Scharfman, H.E., and Hen, R. (2015). Activation of local inhibitory circuits in the dentate gyrus by adult-born neurons. *Hippocampus*. Published online December 14, 2015. <http://dx.doi.org/10.1002/hipo.22557>.
- Espósito, M.S., Piatti, V.C., Lapagne, D.A., Morgenstern, N.A., Ferrari, C.C., Pitossi, F.J., and Schinder, A.F. (2005). Neuronal differentiation in the adult hippocampus recapitulates embryonic development. *J. Neurosci.* 25, 10074–10086.
- Ge, S., Goh, E.L., Sailor, K.A., Kitabatake, Y., Ming, G.L., and Song, H. (2006). GABA regulates synaptic integration of newly generated neurons in the adult brain. *Nature* 439, 589–593.
- Ge, S., Yang, C.H., Hsu, K.S., Ming, G.L., and Song, H. (2007). A critical period for enhanced synaptic plasticity in newly generated neurons of the adult brain. *Neuron* 54, 559–566.
- Gu, Y., Arruda-Carvalho, M., Wang, J., Janoschka, S.R., Josselyn, S.A., Frankland, P.W., and Ge, S. (2012). Optical controlling reveals time-dependent roles for adult-born dentate granule cells. *Nat. Neurosci.* 15, 1700–1706.
- Ikrar, T., Guo, N., He, K., Besnard, A., Levinson, S., Hill, A., Lee, H.K., Hen, R., Xu, X., and Sahay, A. (2013). Adult neurogenesis modifies excitability of the dentate gyrus. *Front. Neural Circuits* 7, 204.
- Imayoshi, I., Sakamoto, M., Ohtsuka, T., Takao, K., Miyakawa, T., Yamaguchi, M., Mori, K., Ikeda, T., Itohara, S., and Kageyama, R. (2008). Roles of continuous neurogenesis in the structural and functional integrity of the adult forebrain. *Nat. Neurosci.* 11, 1153–1161.
- Jia, H., Rochefort, N.L., Chen, X., and Konnerth, A. (2011). In vivo two-photon imaging of sensory-evoked dendritic calcium signals in cortical neurons. *Nat. Protoc.* 6, 28–35.
- Jung, M.W., and McNaughton, B.L. (1993). Spatial selectivity of unit activity in the hippocampal granular layer. *Hippocampus* 3, 165–182.
- Kaifosh, P., Lovett-Barron, M., Turi, G.F., Reardon, T.R., and Losonczy, A. (2013). Septo-hippocampal GABAergic signaling across multiple modalities in awake mice. *Nat. Neurosci.* 16, 1182–1184.
- Kaifosh, P., Zaremba, J.D., Danielson, N.B., and Losonczy, A. (2014). SIMA: Python software for analysis of dynamic fluorescence imaging data. *Front. Neuroinform.* 8, 80.
- Kheirbek, M.A., Klemenhagen, K.C., Sahay, A., and Hen, R. (2012a). Neurogenesis and generalization: a new approach to stratify and treat anxiety disorders. *Nat. Neurosci.* 15, 1613–1620.
- Kheirbek, M.A., Tannenholz, L., and Hen, R. (2012b). NR2B-dependent plasticity of adult-born granule cells is necessary for context discrimination. *J. Neurosci.* 32, 8696–8702.
- Kheirbek, M.A., Drew, L.J., Burghardt, N.S., Costantini, D.O., Tannenholz, L., Ahmari, S.E., Zeng, H., Fenton, A.A., and Hen, R. (2013). Differential control of learning and anxiety along the dorsoventral axis of the dentate gyrus. *Neuron* 77, 955–968.
- Kraus, B.J., Robinson, R.J., 2nd, White, J.A., Eichenbaum, H., and Hasselmo, M.E. (2013). Hippocampal “time cells”: time versus path integration. *Neuron* 78, 1090–1101.
- Kropff, E., Carmichael, J.E., Moser, M.B., and Moser, E.I. (2015). Speed cells in the medial entorhinal cortex. *Nature* 523, 419–424.
- Lacefield, C.O., Itskov, V., Reardon, T., Hen, R., and Gordon, J.A. (2012). Effects of adult-generated granule cells on coordinated network activity in the dentate gyrus. *Hippocampus* 22, 106–116.
- Leal, S.L., Tighe, S.K., Jones, C.K., and Yassa, M.A. (2014). Pattern separation of emotional information in hippocampal dentate and CA3. *Hippocampus* 24, 1146–1155.
- Leutgeb, J.K., Leutgeb, S., Moser, M.B., and Moser, E.I. (2007). Pattern separation in the dentate gyrus and CA3 of the hippocampus. *Science* 315, 961–966.
- Lovett-Barron, M., Kaifosh, P., Kheirbek, M.A., Danielson, N., Zaremba, J.D., Reardon, T.R., Turi, G.F., Hen, R., Zemelman, B.V., and Losonczy, A. (2014). Dendritic inhibition in the hippocampus supports fear learning. *Science* 343, 857–863.
- MacDonald, C.J., Lepage, K.Q., Eden, U.T., and Eichenbaum, H. (2011). Hippocampal “time cells” bridge the gap in memory for discontiguous events. *Neuron* 71, 737–749.

- Madisen, L., Zwingman, T.A., Sunkin, S.M., Oh, S.W., Zariwala, H.A., Gu, H., Ng, L.L., Palmiter, R.D., Hawrylycz, M.J., Jones, A.R., et al. (2010). A robust and high-throughput Cre reporting and characterization system for the whole mouse brain. *Nat. Neurosci.* 13, 133–140.
- Madisen, L., Mao, T., Koch, H., Zhuo, J.M., Berenyi, A., Fujisawa, S., Hsu, Y.W., Garcia, A.J., 3rd, Gu, X., Zanella, S., et al. (2012). A toolbox of Cre-dependent optogenetic transgenic mice for light-induced activation and silencing. *Nat. Neurosci.* 15, 793–802.
- Marín-Burgin, A., Mongiat, L.A., Pardi, M.B., and Schinder, A.F. (2012). Unique processing during a period of high excitation/inhibition balance in adult-born neurons. *Science* 335, 1238–1242.
- Nakashiba, T., Cushman, J.D., Pelkey, K.A., Renaudineau, S., Buhl, D.L., McHugh, T.J., Rodriguez Barrera, V., Chittajallu, R., Iwamoto, K.S., McBain, C.J., et al. (2012). Young dentate granule cells mediate pattern separation, whereas old granule cells facilitate pattern completion. *Cell* 149, 188–201.
- Neunuebel, J.P., and Knierim, J.J. (2012). Spatial firing correlates of physiologically distinct cell types of the rat dentate gyrus. *J. Neurosci.* 32, 3848–3858.
- Paninski, L. (2003). Estimation of entropy and mutual information. *Neural Comput.* 15, 1191–1253.
- Park, E.H., Burghardt, N.S., Dvorak, D., Hen, R., and Fenton, A.A. (2015). Experience-dependent regulation of dentate gyrus excitability by adult-born granule cells. *J. Neurosci.* 35, 11656–11666.
- Pernia-Andrade, A.J., and Jonas, P. (2014). Theta-gamma-modulated synaptic currents in hippocampal granule cells *in vivo* define a mechanism for network oscillations. *Neuron* 81, 140–152.
- Piatti, V.C., Ewell, L.A., and Leutgeb, J.K. (2013). Neurogenesis in the dentate gyrus: carrying the message or dictating the tone. *Front. Neurosci.* 7, 50.
- Restivo, L., Niibori, Y., Mercaldo, V., Josselyn, S.A., and Frankland, P.W. (2015). Development of adult-generated cell connectivity with excitatory and inhibitory cell populations in the hippocampus. *J. Neurosci.* 35, 10600–10612.
- Sahay, A., Scobie, K.N., Hill, A.S., O'Carroll, C.M., Kheirbek, M.A., Burghardt, N.S., Fenton, A.A., Dranovsky, A., and Hen, R. (2011a). Increasing adult hippocampal neurogenesis is sufficient to improve pattern separation. *Nature* 472, 466–470.
- Sahay, A., Wilson, D.A., and Hen, R. (2011b). Pattern separation: a common function for new neurons in hippocampus and olfactory bulb. *Neuron* 70, 582–588.
- Santarelli, L., Saxe, M., Gross, C., Surget, A., Battaglia, F., Dulawa, S., Weisstaub, N., Lee, J., Duman, R., Arancio, O., et al. (2003). Requirement of hippocampal neurogenesis for the behavioral effects of antidepressants. *Science* 301, 805–809.
- Schmidt-Hieber, C., Jonas, P., and Bischofberger, J. (2004). Enhanced synaptic plasticity in newly generated granule cells of the adult hippocampus. *Nature* 429, 184–187.
- Schmidt-Hieber, C., Wei, H., and Häusser, M. (2014). Synaptic mechanisms of sparse activity in hippocampal granule cells during mouse navigation (Society for Neuroscience).
- Singer, B.H., Gamelli, A.E., Fuller, C.L., Temme, S.J., Parent, J.M., and Murphy, G.G. (2011). Compensatory network changes in the dentate gyrus restore long-term potentiation following ablation of neurogenesis in young-adult mice. *Proc. Natl. Acad. Sci. USA* 108, 5437–5442.
- Skaggs, W.E., McNaughton, B.L., Gothard, K.M., and Markus, E.J. (1993). An information-theoretic approach to deciphering the hippocampal code. In *Advances in Neural Information Processing Systems (NIPS)*, 5, S.J. Hanson, J.D. Cowan, and C.L. Giles, eds, pp. 1030–1037.
- Snyder, J.S., Soumier, A., Brewer, M., Pickel, J., and Cameron, H.A. (2011). Adult hippocampal neurogenesis buffers stress responses and depressive behaviour. *Nature* 476, 458–461.
- Spalding, K.L., Bergmann, O., Alkass, K., Bernard, S., Salehpour, M., Huttner, H.B., Boström, E., Westerlund, I., Vial, C., Buchholz, B.A., et al. (2013). Dynamics of hippocampal neurogenesis in adult humans. *Cell* 153, 1219–1227.
- Stone, S.S., Teixeira, C.M., Zaslavsky, K., Wheeler, A.L., Martinez-Canabal, A., Wang, A.H., Sakaguchi, M., Lozano, A.M., and Frankland, P.W. (2011). Functional convergence of developmentally and adult-generated granule cells in dentate gyrus circuits supporting hippocampus-dependent memory. *Hippocampus* 21, 1348–1362.
- Temprana, S.G., Mongiat, L.A., Yang, S.M., Trinchero, M.F., Alvarez, D.D., Kropff, E., Giacomini, D., Beltramone, N., Lanuza, G.M., and Schinder, A.F. (2015). Delayed coupling to feedback inhibition during a critical period for the integration of adult-born granule cells. *Neuron* 85, 116–130.
- Toni, N., Teng, E.M., Bushong, E.A., Aimone, J.B., Zhao, C., Consiglio, A., van Praag, H., Martone, M.E., Ellisman, M.H., and Gage, F.H. (2007). Synapse formation on neurons born in the adult hippocampus. *Nat. Neurosci.* 10, 727–734.
- Toni, N., Laplagne, D.A., Zhao, C., Lombardi, G., Ribak, C.E., Gage, F.H., and Schinder, A.F. (2008). Neurons born in the adult dentate gyrus form functional synapses with target cells. *Nat. Neurosci.* 11, 901–907.
- van Praag, H., Schinder, A.F., Christie, B.R., Toni, N., Palmer, T.D., and Gage, F.H. (2002). Functional neurogenesis in the adult hippocampus. *Nature* 415, 1030–1034.
- Yassa, M.A., Mattfeld, A.T., Stark, S.M., and Stark, C.E. (2011). Age-related memory deficits linked to circuit-specific disruptions in the hippocampus. *Proc. Natl. Acad. Sci. USA* 108, 8873–8878.
- Zhao, C., Deng, W., and Gage, F.H. (2008). Mechanisms and functional implications of adult neurogenesis. *Cell* 132, 645–660.
- Ziv, Y., Burns, L.D., Cocker, E.D., Hamel, E.O., Ghosh, K.K., Kitch, L.J., El Gamal, A., and Schnitzer, M.J. (2013). Long-term dynamics of CA1 hippocampal place codes. *Nat. Neurosci.* 16, 264–266.

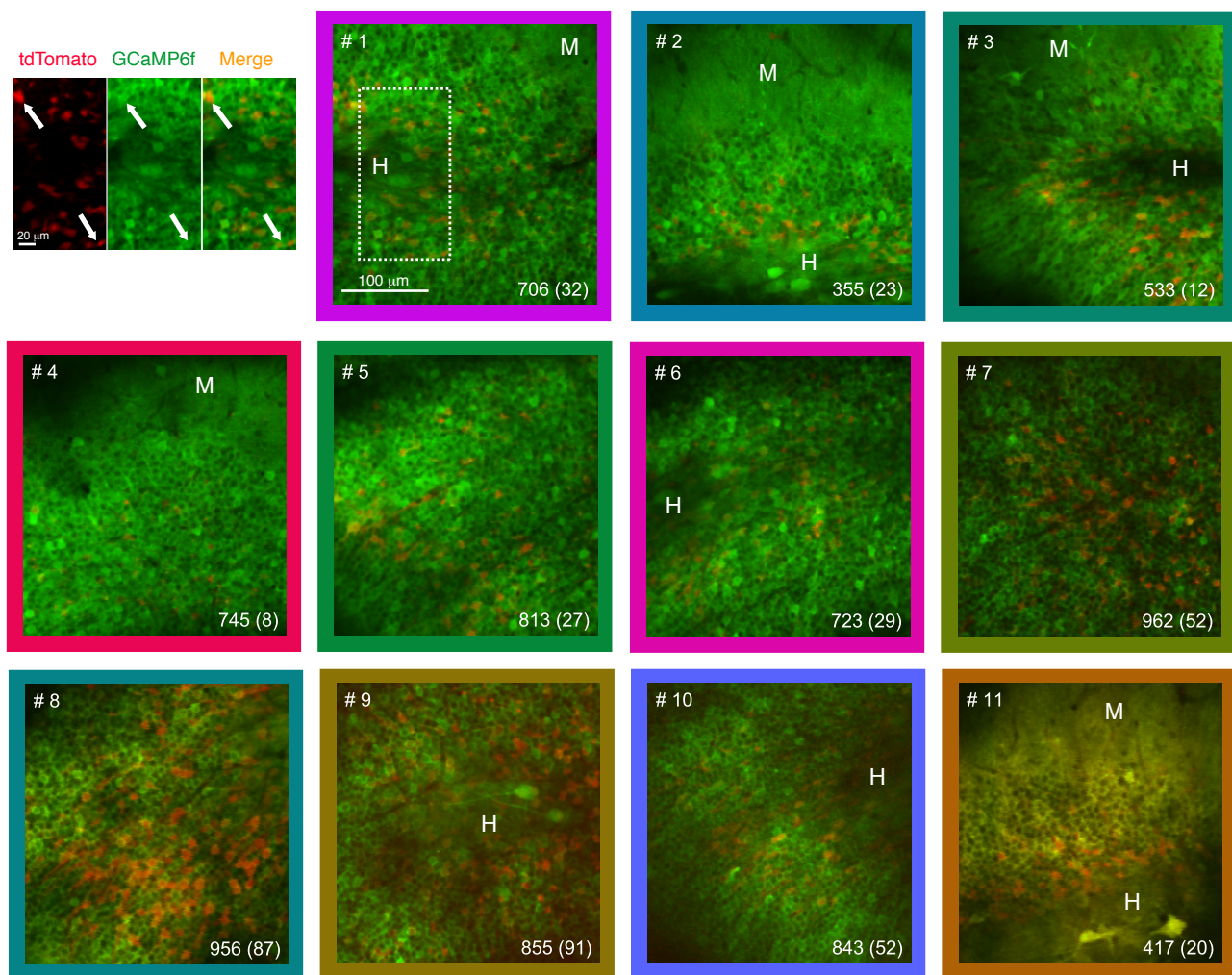
Supplemental Information

**Distinct Contribution of Adult-Born
Hippocampal Granule Cells to Context Encoding**

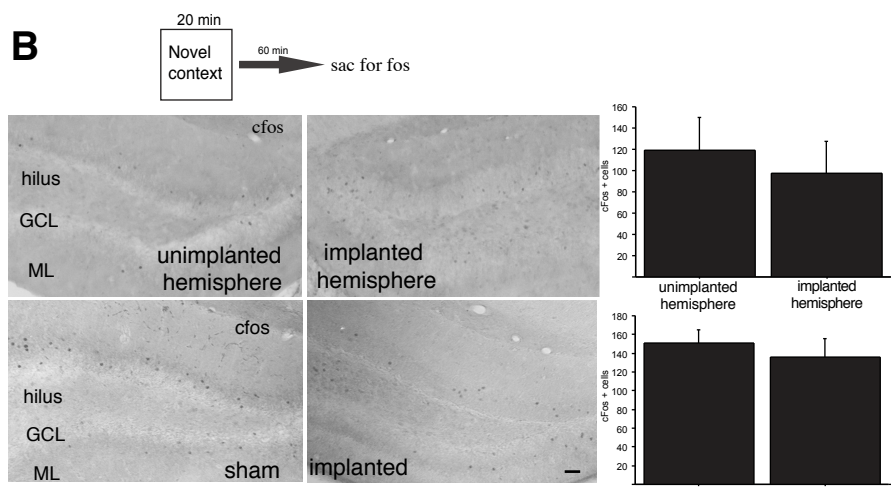
Nathan B. Danielson, Patrick Kaifosh, Jeffrey D. Zaremba, Matthew Lovett-Barron, Joseph Tsai, Christine A. Denny, Elizabeth M. Balough, Alexander R. Goldberg, Liam J. Drew, René Hen, Attila Losonczy, and Mazen A. Kheirbek

Supplemental figure 1

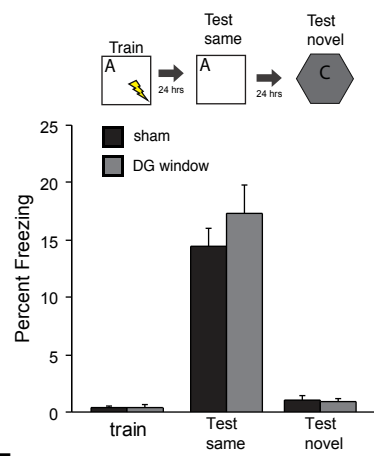
A



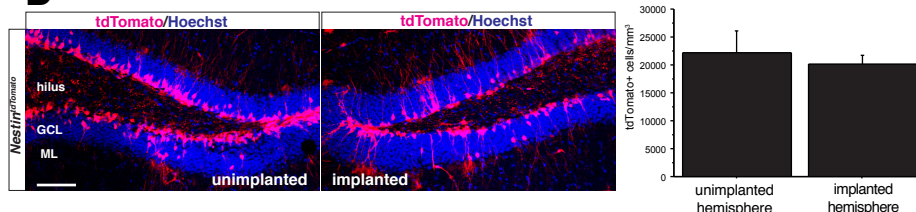
B



C



D



E

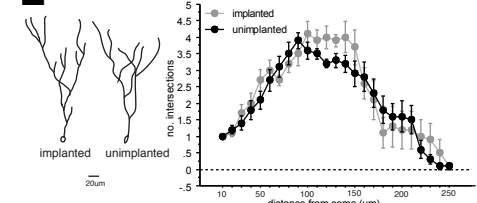


Figure S1, related to Figure 1: *In vivo* Ca²⁺ imaging of DG GCs

(a) Images of all fields of view during 2P DG imaging. The FOV from which the example cells in Fig. 2A,B were drawn. Arrows mark the location of the example newborn (tdTomato-positive) and mature (tdTomato-negative) cell. The corresponding area is shown in FOV #1. The numbers in each FOV indicate the number of mGCs (719 ± 204 , mean \pm s.d., n = 11 FOVs) and abGCs (39 ± 28 , mean \pm s.d., n = 11 FOVs) identified. The border color around each FOV matches the color scheme used through the figures. In some fields the two-photon imaging plane passes through the hilar (H) or molecular layers (M) as a consequence of the curved 3D geometry of the dentate gyrus dorsal blade. **(b-c)** Window implantation does not impact overall DG activity or hippocampus-dependent contextual fear conditioning. **(b)** Implanted mice explored a novel context for 20 min and were sacrificed for cFos immunohistochemistry 60 minutes later. The number of cFos+ cells in the GCL did not differ between the implanted and unimplanted hemisphere (n=4, unpaired t-test, $t_6=-0.5$, p=0.64). In addition, cFos+ cells did not differ between implanted and sham mice n=3-4/condition, unpaired t-test, $t_5=-0.6$, p=0.57) (scale bar=100um). **(c)** Window implantation did not impact one-trial contextual fear conditioning (n=8 sham, 7 DG window, group effect $F_{(1,13)}=0.9$, p=0.36, training effect $F_{(1,13)}=113.9$, p<0.001 group X training interaction $F_{(1,13)}=0.93$, p=0.35 (on test same context $t_{13}=-.9$, p=0.34). In addition, mice with window implantation could discriminate between different contexts (group effect $F_{(1,26)}=0.9$, p=0.36, context effect $F_{(1,26)}=1635$, p<0.001 group X context interaction $F_{(1,26)}=17.3$, p=0.32). **(d)** Window implantation did not impact total number of six week old and younger tdTomato+ abGCs in the implanted hemisphere (n=6 unpaired t-test, $t_6=-0.6$, p=0.59). **(e)** We conducted analysis on the dendrites of abGCs in the implanted and unimplanted hemispheres, and did not detect significant differences in the dendritic architecture of neurons on the implanted side (n=10/side, repeated measures ANOVA, intersection X hemisphere interaction $F_{(24,432)}=1.2$, p=0.23). We also determined the number of proliferating neurons, as measured by Ki67 immunohistochemistry, and did not detect differences (data not shown; n=4/group, $t_6=-2.1$, p=0.1).

Supplemental figure 2

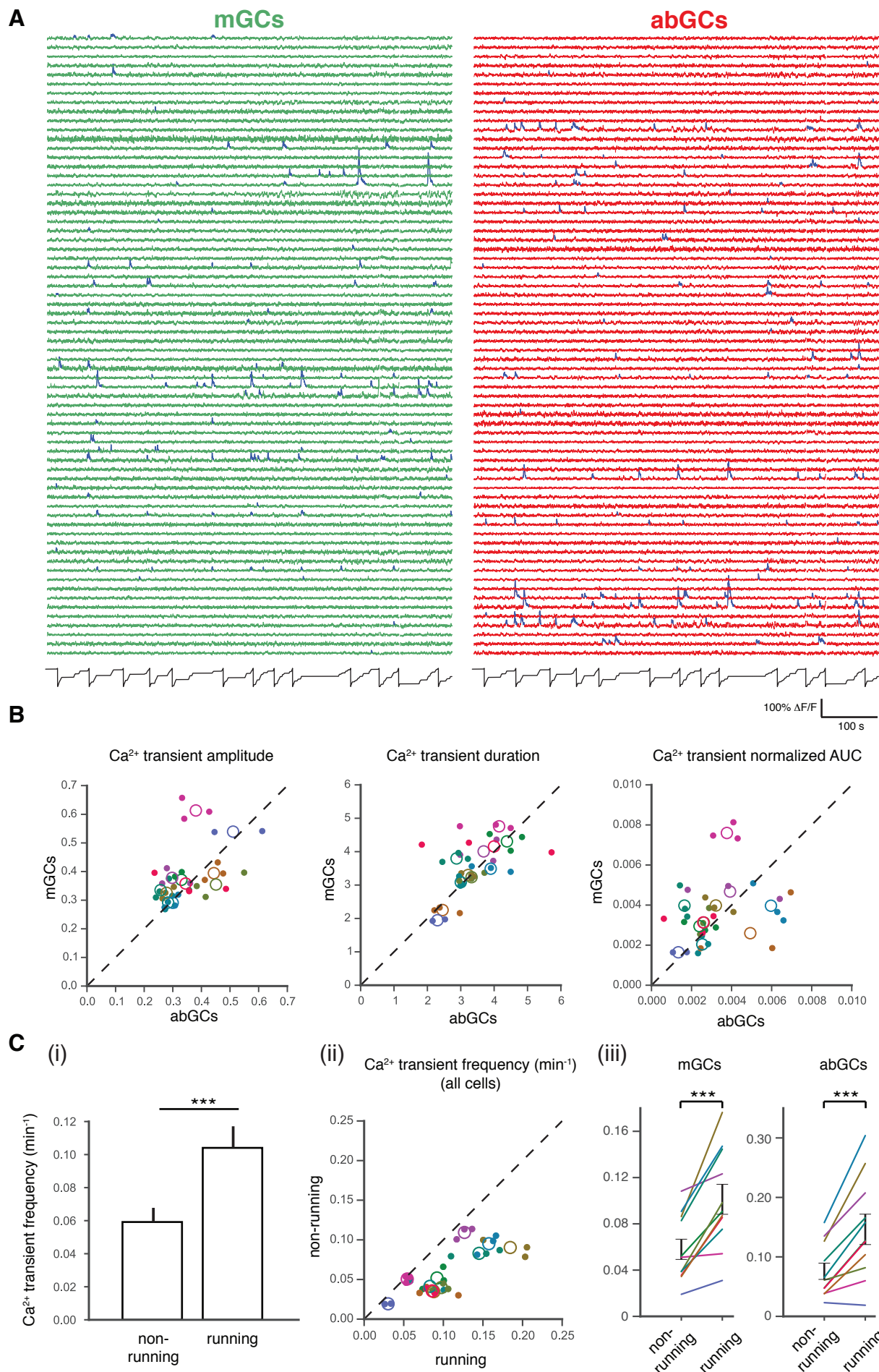


Figure S2, related to Figure 2. Population activity in DG GCs during behavior

(a) Example traces and transient detection. For a single 12-minute recording session we plotted the processed df/f Ca^{2+} trace for all newborn neurons in the FOV and for an equal number of randomly sampled mGCs. Statistically significant Ca^{2+} transients ($p < 0.05$) are indicated in blue, and the mouse's position in this experiment is plotted in black at bottom. **(b)** Activity comparison plots. As plotted in Fig 1D, for all cells imaged we computed the mean amplitude, duration, and transient AUC (total area under DF/F curve during significant transients) across recordings. Data is plotted by averaging mature and newborn subpopulations across experiments (closed circles) and FOVs (open circles). Across FOVs and cells, we did not detect differences between mGCs and abGCs in the amplitude or duration of calcium transients (2-sample paired T-Test; $n=11$ FOV; $p=0.21$, 0.45 , and 0.42 for amplitude, duration, and transient AUC, respectively). **(c)** Non-running vs. running analysis. *(i)* Mean Ca^{2+} transient frequency with onset during non-running and running-related imaging frames. Across fields of view, running-related transients are observed at a significantly higher rate during running than during non-running epochs (non-running: 0.06 ± 0.01 transients/min.; running: 0.10 ± 0.01 transients/min.; $t=-5.66$; $p<0.001$; $n=10$ FOV; paired T-Test). *(ii)* Scatter of mean running-related and non-running-related Ca^{2+} transient frequency by recording (closed circles) and by FOV (open circles). Color as in Fig S1. *(iii)* Data aggregated by FOV separately for mGCs and for abGCs. Both populations showed higher activity during running than non-running periods (mGCs: non-running: 0.06 ± 0.01 transients/min.; running: 0.10 ± 0.01 transients/min.; $t=-5.60$; $p<0.001$; $n=11$ FOV; paired T-Test; abGCs: non-running: 0.08 ± 0.01 transients/min.; running: 0.15 ± 0.03 transients/min.; $t=-5.16$; $p<0.001$; $n=11$ FOV; paired T-Test).

Supplemental figure 3

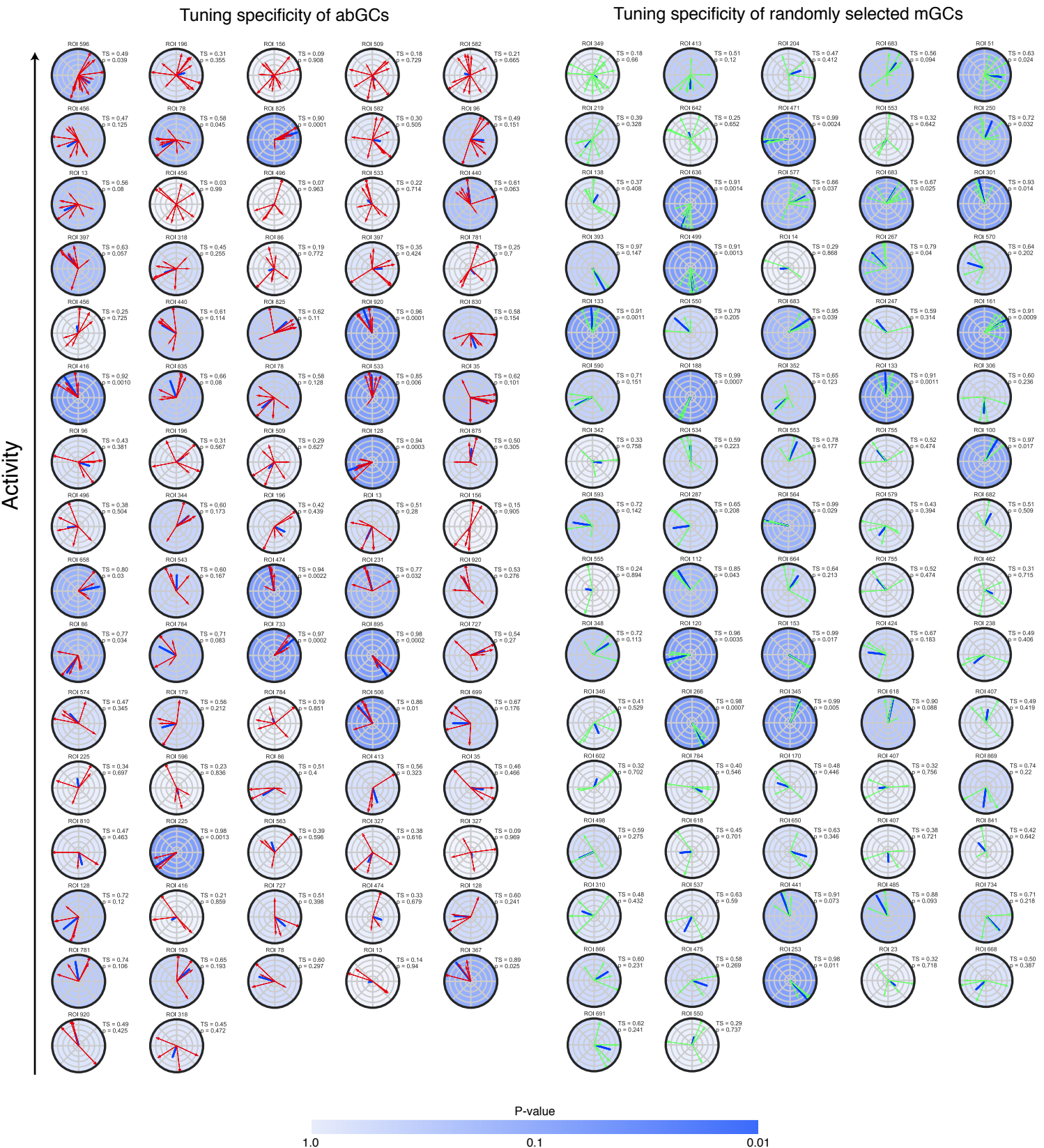


Figure S3, related to Figure 2. Tuning direction plots of abGCs and mGCs

For every abGC firing at least four significant transients, we plotted the direction of every running-related transient as well as the overall tuning direction (dark blue line). Vectors are inversely weighted by occupancy and normalized to peak. Tuning strength (*TS*) and associated p-value is indicated for each cell. P-values are calculated relative to the expected distribution for an equal number of running-related transients randomly distributed in time (see Methods). The blue background shading is a reflection of the tuning specificity p-value. Color intensity is logarithmically related to the p-value. B) For random sampled mature granule cells firing with least four significant transients, we plotted the direction of every running-related transient as well as the overall tuning direction (dark blue line). Vectors are inversely weighted by occupancy and normalized to peak. Tuning strength (*TS*) and associated p-value is indicated for each cell. P-values are calculated relative to the expected distribution for an equal number of running-related transients randomly distributed in time (see Methods). The blue background shading is a reflection of the tuning specificity p-value. Color intensity is logarithmically related to the p-value.

Supplemental figure 4

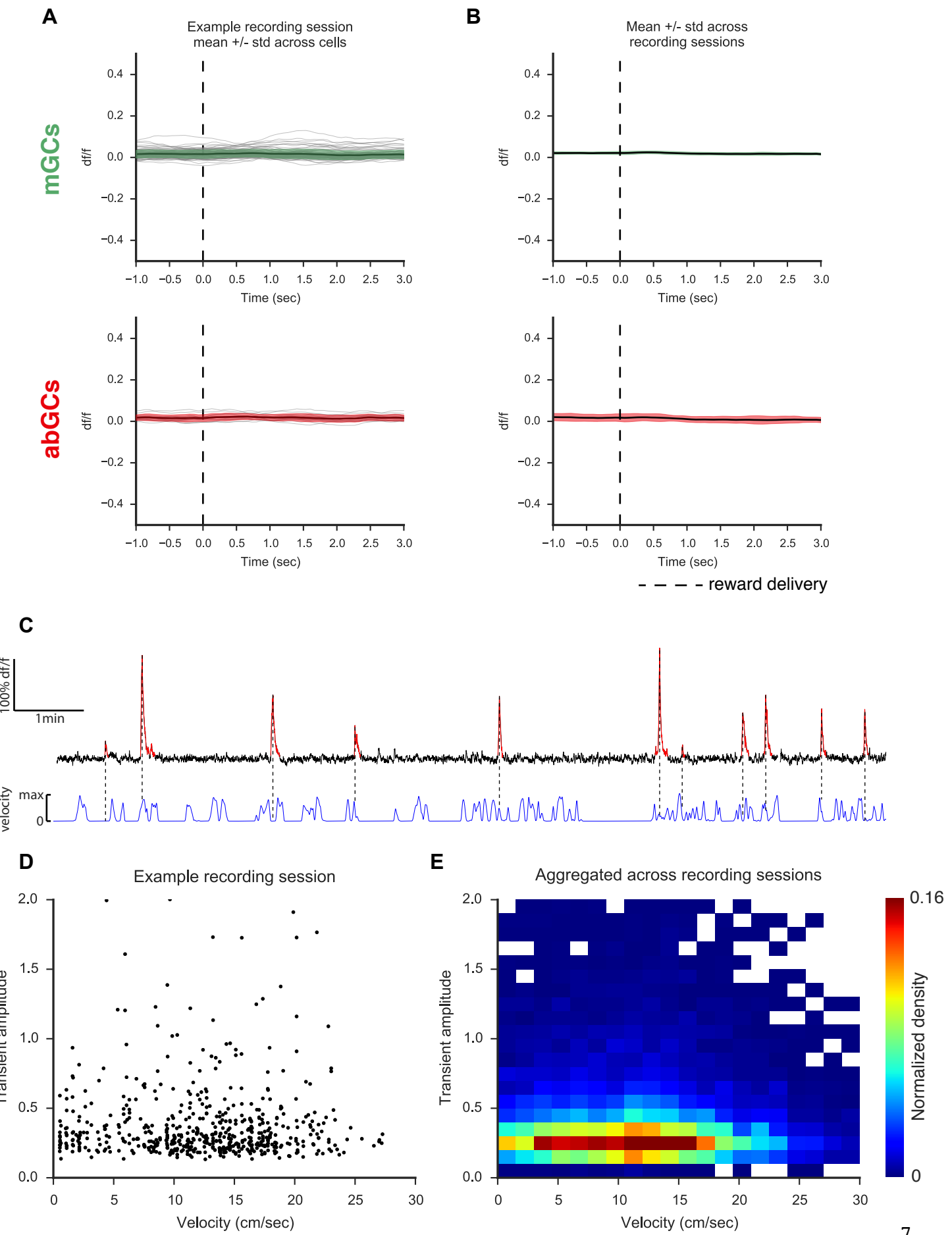
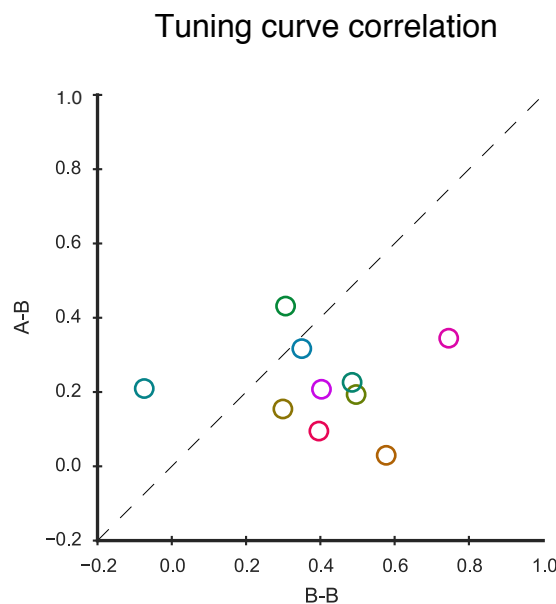


Figure S4, related to Figure 2. Reward and velocity-related responses

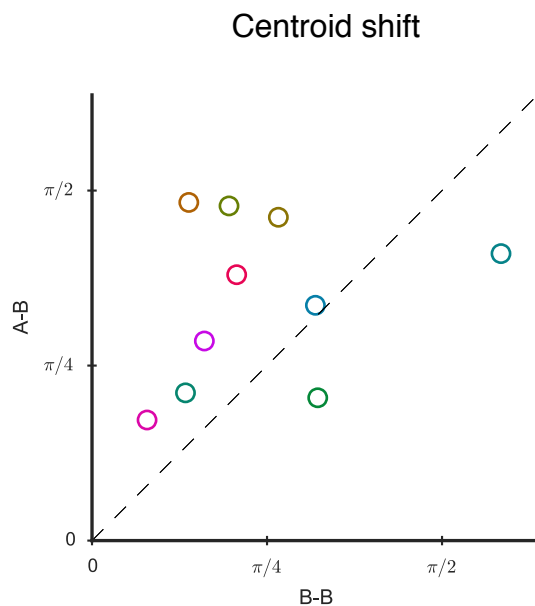
(a-b) For each cell we calculated a peri-stimulus time histogram (PSTH) for GCaMP6f fluorescence triggered on the delivery of the water rewards. Because so many of the granule cells are silent, we included only active cells in this analysis (at least 4 Ca²⁺ transients). **(a)** Data from active cells in a single experiment. mGCs and abGCs are on top and bottom respectively. Light gray traces reflect the PSTH's of individual cells in the recording (n=92 mGCs, n=13 abGCs). Shaded region is the mean +/- the standard deviation of the Ca²⁺ responses. Three randomly placed rewards were administered per lap. PSTHs are based on all reward presentations in the experiment. **(b)** Mean +/- the standard deviation of the means for each recording session (n=32 recordings). In none of our recordings did we find a significant reward response. **(c-d)** In order to determine if activity is related to velocity, it is necessary to estimate a continuous firing rate, which can then be correlated with the animal's velocity (Kropff et al., 2015). Estimating a continuous firing rate from calcium imaging data is difficult, however, and is not possible in context of very low transient rates, as were observed in this study. The best proxy we have for spike rate is the amplitude of the detected transients (large transients reflect large bursts of spikes, while small transients reflect fewer numbers of spikes). If there were a relationship between activity and velocity, then large amplitude events should be associated with faster velocities and vice versa. For this analysis we included only transients associated with a non-zero velocity to maximize our likelihood of detecting a relationship. **(c)** Top: df/f Ca²⁺ trace from an example cell. Significant transients ($p < 0.05$) in red. Bottom: The mouse's velocity over the course of the same 10min trial. **(d)** Scatter plot of transient amplitude vs. the mouse's velocity at the time of transient onset. There was no relationship between amplitude and velocity (Pearson $r = -0.009$, $p = 0.81$). **(e)** Data was combined across all recording sessions and a 2D-histogram was calculated. Color indicates the density of transients in each bin. Upper and lower colormap values represent the 1st and 99th percentiles of the density distribution.

Supplemental figure 5

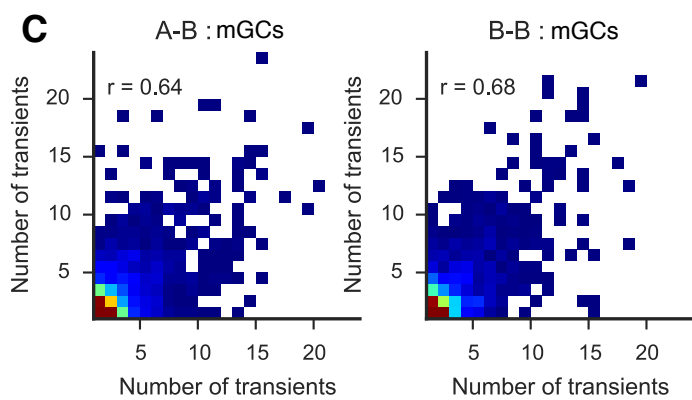
A



B



C



D

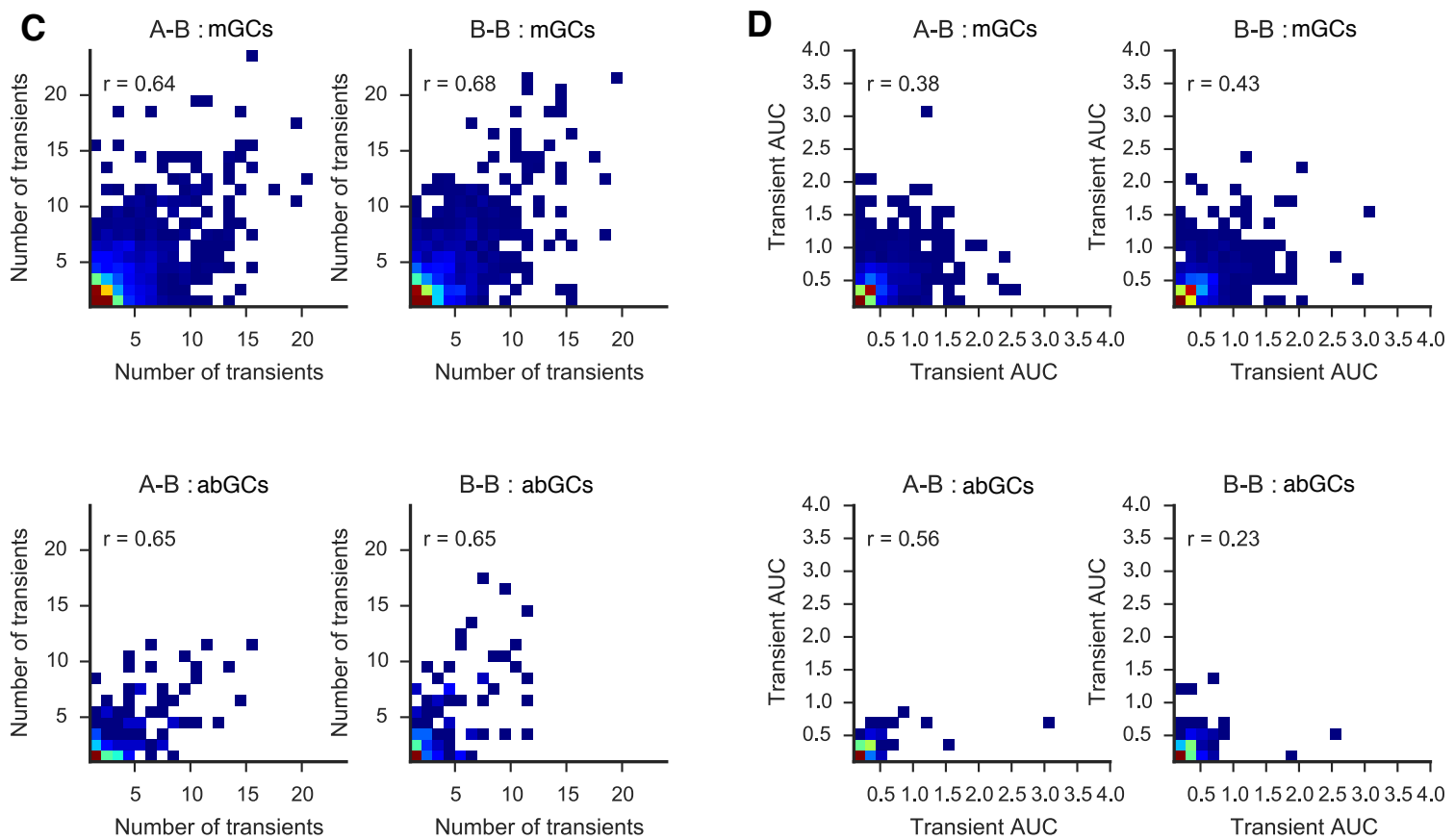


Figure S5, related to Figures 3-5. Remapping dynamics

Tuning curve correlations (**a**) and centroid shift (**b**) assessed by averaging across mGCs within each FOV. mGCs in 8/10 FOVs maintained significantly more similar spatial representations in the A-A condition than in the A-B condition (paired two-sided T-Test; n=10, **b**, $T_{(18)} = 2.27$, $p < 0.05$; **c**, $T_{(18)} = -1.97$, $p = 0.07$). (**c-d**) In order to assess encoding of context through overall activity throughout the trial, we plotted the total number of transients (**c**) and mean transient AUC (total area under all significant transients; **d**) in one trial as a function of the activity in the next trial. This two-dimensional data was binned, and a normalized 2D-histogram was calculated. Upper and lower colormap values represent the 1st and 99th percentiles of the density distribution. The relationship between trial-to-trial activity in the ‘B-B’ condition appears similar as that of the ‘A-B’ condition, supporting our analysis in **Fig 6**. Data is plotted separately for newborn (*bottom*) and mature (*top*) cells and for the ‘A-B’ (*left*) and ‘B-B’ (*right*) conditions.

Supplemental figure 6

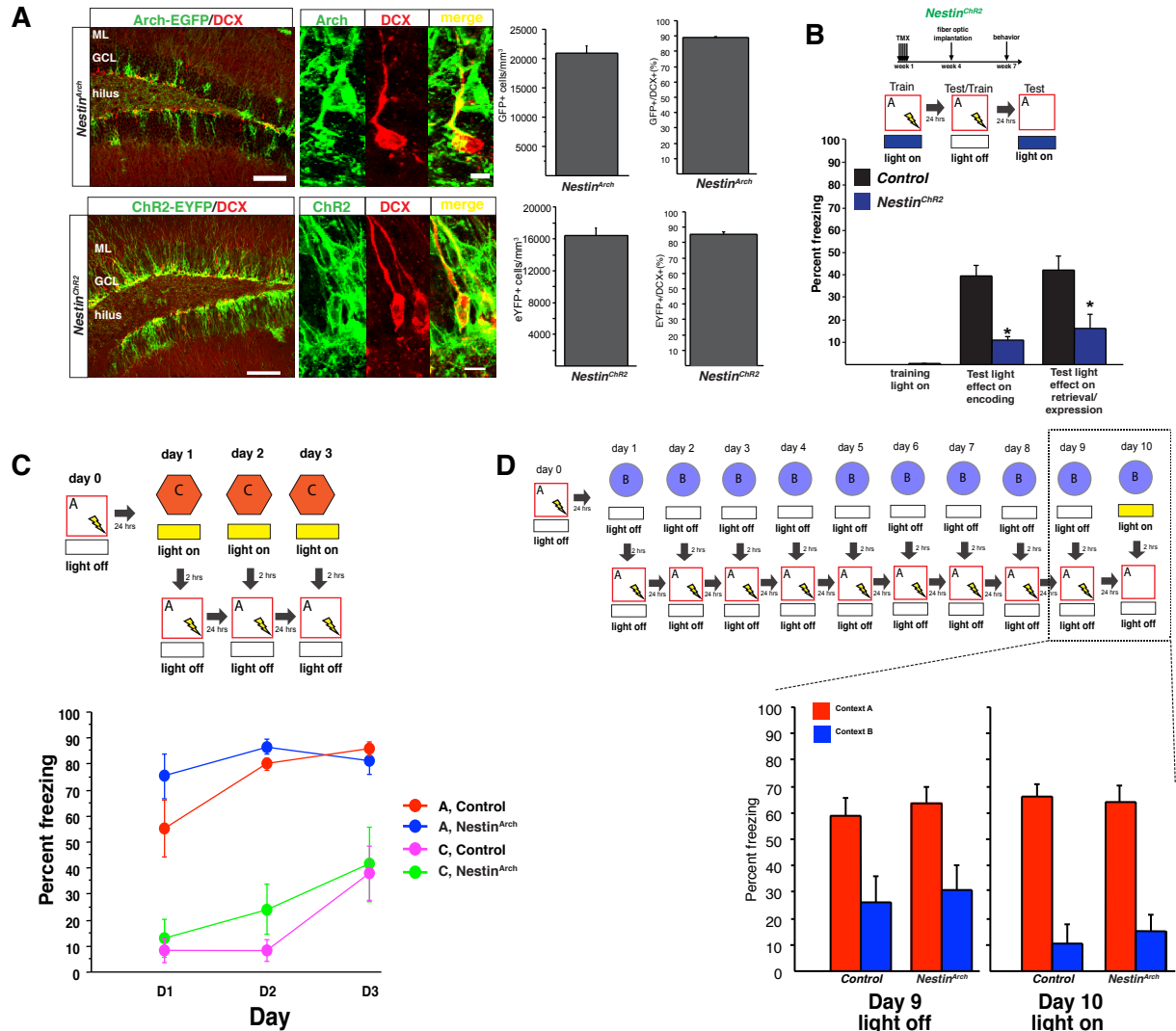


Figure S6, related to Figure 6. Optogenetic modulation of abGCs.

(a) Expression of opsins in abGCs. TMX induction was performed as described in the Methods. In the DG of *Nestin^{Arch}* and *Nestin^{ChR2}* mice, the majority of DCX+ cells expressed opsins (n=3-4/geno *Nestin^{Arch}*: 88.9 +/- 2.9%, n=3-4/geno, *Nestin^{ChR2}*: 85.4+/- 2.9% of the DCX population of immature cells). (Scale bars 100um (low mag) and 10um (high mag)) **(b)** Stimulation of abGCs in the dorsal DG impairs encoding and retrieval of fear memories (n=9 control, 8 *Nestin^{ChR2}*, group effect $F_{(1,15)}=11.12$, p=0.005, group X training interaction $F_{(1,14)}=24.4$, p=0.0064 (on test off day $t_{14}=5$, p<0.01, on test on day $t_{14}=2.9$, p=0.01). **(c)** Inhibition of abGCs during exposure to a highly dissimilar context does not impair discrimination. (n=5 control, 4 *Nestin^{Arch}*, group effect $F_{(1,14)}=1.5$, p=0.23, context effect $F_{(1,14)}=78.9$, p<0.001, day effect $F_{(2,28)}=17.4$, p<0.001, groupXdayXcontext effect $F_{(2,28)}=1.5$, p=0.24.) This ability to discriminate may also be due to the fact that young neurons were not required to associate the tactile cues of the bars with the delivery of the footshock. **(d)** Inhibition of abGCs does not impair the expression of contextual fear discrimination. Mice were trained to discriminate between two similar contexts then tested for light effects in the similar context after the discrimination had already been learned. *Nestin^{Arch}* and control mice learned the discrimination task in the absence of light stimulation indicating that TMX or gene expression does not impact discrimination learning (n=7 control 8 *Nestin^{Arch}*, group effect $F_{(1,26)}=3.5$, p=0.1, context effect $F_{(1,26)}=10.2$, p=0.004, day effect $F_{(8,208)}=15.2$, p<0.001, groupXdayXcontext effect $F_{(8,208)}=0.1$, p=0.52. Control: context effect $F_{(1,12)}=4.8$, p=0.02, dayXcontext interaction $F_{(8,96)}=2.2$, p<0.01. *Nestin^{Arch}*: context effect $F_{(1,14)}=5.9$, p=0.04, day X context effect $F_{(8,112)}=2.1$, p=0.04). Yellow light inhibition did not impact fear discrimination (repeated measures ANOVA, group effect $F_{(1,26)}=.2$, p=0.64, context effect $F_{(1,26)}=43.9$, p<0.001, group X context interaction $F_{(1,26)}=0.1$, p=0.8, group X context X day $F_{(1,26)}=0.3$, p=0.59. Error bars are mean +/- SEM

<i>cohort</i>	<i>implant location</i>	<i>test</i>	<i>conditions</i>	<i>stats</i>
Nestin Arch	dorsal DG	shock reactivity	0.75 mA shock	n=8-9/treatment, $t_{15}=0.9$, p=0.4
Nestin Arch	ventral DG	CFC	Light on encoding, light off test, retrain light off, test retrieval light on	n=8-11/treatment, treatment effect $F_{(1,17)}=0.56$, p=0.46, treatment X training interaction $F_{(1,17)}=0.46$, p=0.5 (on test off day $t_{17}=-0.72$, p=0.48, on test on day $t_{17}=-0.75$, p=0.46)
Nestin ChR2	ventral DG	CFC	Light on encoding, light off test, retrain light off, test retrieval light on	n=8-10/treatment, treatment effect $F_{(1,16)}=2.4$, p=0.14, treatment X training interaction $F_{(1,16)}=2.2$, p=0.2 (on test off day $t_{16}=-1.5$, p=0.15, on test on day $t_{16}=-0.15$, p=0.9)
Nestin Arch	dorsal DG	OFT	5min light off, 5min light on, 5min light off	n=8-9/ geno, total distance traveled, genotype effect $F_{(1,15)}=1.3$, p=0.1, genoXlight effect $F_{(2,30)}=0.4$, p=0.7, percent center distance: genotype effect $F_{(1,15)}=0.9$, p=0.4, genoXlight effect $F_{(2,30)}=2.3$, p=0.1
Nestin Arch	dorsal DG	EPM	5min light off, 5min light on, 5min light off	n=8/geno, total distance traveled genotype effect $F(1,14)=0.4$, p=0.6, genoXlight effect $F(2,28)=1.2$, p=0.3; time in open arms genotype effect $F_{(1,14)}=1.3$, p=0.3, genoXlight effect $F_{(2,28)}=1.8$, p=0.2.
Nestin Arch	ventral DG	OFT	5min light off, 5min light on, 5min light off	n=8-11/geno, total distance traveled (genotype effect $F_{(1,17)}=1.7$, p=0.2, genoXlight effect $F_{(2,34)}=1.2$, p=0.3, percent center distance: genotype effect $F_{(1,17)}=0.3$, p=0.6, genoXlight effect $F_{(2,34)}=0.6$, p=0.5)
Nestin Arch	ventral DG	EPM	5min light off, 5min light on, 5min light off	n=8-9/geno, total distance traveled genotype effect $F(1,15)=4$, p=0.06, genoXlight effect $F(2,30)=0.3$, p=0.8; time in open arms, genotype effect $F_{(1,15)}=1.2$, p=0.3, genoXlight effect $F_{(2,30)}=1.2$, p=0.3.
Nestin ChR2	dorsal DG	OFT	5min light off, 5min light on, 5min light off	n=7-9/ geno, total distance traveled, genotype effect $F_{(1,14)}=1.1$, p=0.3, genoXlight effect $F_{(2,28)}=3.3$, p=0.05, percent center distance: genotype effect $F_{(1,14)}=0.5$, p=0.5, genoXlight effect $F_{(2,28)}=2.3$, p=0.1
Nestin ChR2	dorsal DG	EPM	5min light off, 5min light on, 5min light off	n=7-8/geno, total distance traveled genotype effect $F(1,13)=0.7$, p=0.4, genoXlight effect $F(2,26)=4.8$, p=0.02, time in open arms, genotype effect $F_{(1,13)}=0.4$, p=0.6, genoXlight effect $F_{(2,26)}=0.6$, p=0.6.
Nestin ChR2	ventral DG	OFT	5min light off, 5min light on, 5min light off	n=9-10/geno, total distance traveled, genotype effect $F_{(1,17)}=1.1$, p=0.3, genoXlight effect $F_{(2,34)}=0.4$, p=0.7, percent center distance: genotype effect $F_{(1,17)}=0.9$, p=0.3, genoXlight effect $F_{(2,34)}=0.1$, p=0.9
Nestin ChR2	ventral DG	EPM	5min light off, 5min light on, 5min light off	n=9-10/geno ,total distance traveled genotype effect $F(1,17)=1.8$, p=0.2, genoXlight effect $F(2,34)=1.5$, p=0.2; time in open arms, genotype effect $F_{(1,17)}=0.3$, p=0.6, genoXlight effect $F_{(2,34)}=0.8$, p=0.5,

Table S1, related to Figure 6. Control behavioral experiments. Table contains results from behavioral experiments for effects of inhibition or excitation of abGCs in anxiety-like behavior, shock reactivity and contextual fear conditioning. (CFC- contextual fear conditioning, OFT- Open Field Test, EPM- Elevated Plus Maze)

Movie S1, related to Figure 1. Sparse granule cell population activity. 5 minutes of GCaMP6f activity in the behaving mouse (300 x 300 μ m FOV, ~1000 cells) played at 10x speed (30sec total). Frames were smoothed with $\sigma=3$ pixels, compressed as MPEG, and edited in iMovie. Transients are observed at extremely low rates (see **Fig 2**).

Supplemental Experimental Procedures

Mice:

All experiments were conducted in accordance with the US National Institutes of Health guidelines and with the approval of the Columbia University and New York State Psychiatric Institute Institutional Animal Care and Use Committees.

Male *ROSA26-CAG-stop^{flx}-ChR2(H134R)-eYFP* (*Ai32*), *ROSA26-CAG-stop^{flx}-Arch-GFP* (*Ai35*), *ROSA26-CAG-stop^{flx}-tDTomato* (*Ai9*) and Nestin-CreER^{T2} (Dranovsky et al., 2011; Madisen et al., 2012; Madisen et al., 2010) and controls were generated as previously described (on mixed background). Mice were housed in the vivarium on a 12-h light/dark cycle and were housed 3-5 mice in each cage (with genotypes/treatments randomized in each cage). Experiments were performed during the light portion of the cycle.

Imaging window implant:

Recombinant adeno-associated viruses carrying the GCaMP6f gene were obtained from the Penn Vector Core (AAV1.Syn.GCaMP6f.WPRE.SV40) with titer of $2\text{-}4 \times 10^{13}$. The dorsal dentate gyrus was stereotactically injected with 3-fold diluted virus (in artificial CSF) using a Nanoject syringe, as described in previously (Kaifosh et al., 2013; Lovett-Barron et al., 2014). Injection coordinates were -1.5 mm AP, -2.3 mm ML, and -1.8, -1.65, -1.5 mm DV relative to the cortical surface. 60 nL of diluted virus was injected at each DV location in 10 nL increments. Mice were then surgically implanted with an imaging window (diameter: 1.5-mm; height: 2.2-mm) over the left dorsal dentate gyrus and implanted with a stainless-steel headpost for head fixation during imaging experiments. Imaging cannulas were constructed by adhering (Narland optical adhesive) a 3-mm glass coverslip (64-0720, Warner) to a cylindrical steel cannula (1.5-mm diameter x 2.3-mm height) and polishing down the overhanging glass with a diamond file. We used a modified version of the same headpost described previously (Kaifosh et al., 2013; Lovett-Barron et al., 2014), in which the posterior bar was thinned to accommodate the 3.5mm working distance of the objective. The surgical procedure was very similar to that previously described, except that the imaging window was implanted 100-200 mm above the hippocampal fissure, providing optical access to the granule cells in the dorsal blade of the DG. Following induction of anesthesia (Isoflurane: 3% induction, 1.5-2.0% maintenance; 1.0 L/min O₂) and administration of analgesia (buprenorphine 0.05-0.1mg/kg), the scalp was removed, and a 1.5 mm diameter craniotomy was performed with a fine-tipped dental drill (V00033, Henry-Schein). The dura was removed, and the underlying cortex was aspirated to reveal the capsular fibers. Following this, a 30g blunt syringe (B30-50, SAI) was used to gently aspirate CA1 directly superior to the dentate until the loose fibers and vasculature of *stratum moleculare* were visible. Bleeding was controlled with a collagen gel sponge (A00063, Avitene) and continuous irrigation with aCSF. We then gently fit the cannula into the craniotomy and affixed the headpost to the skull using dental cement (675572, Dentsply). Mice were active within 15 minutes of surgery, and analgesia was continued for three days post-operatively.

Fiber optic construction and implantation.

Male mice (8 weeks of age) were surgically implanted with fiber optic cannulas at 3 weeks after TMX induction, using published protocols (Kheirbek et al., 2013), and behavioral experiments commenced >3 wks after surgery to allow for recovery. Briefly, a 200um core, 0.37 numerical aperture (NA) multimode fiber (ThorLabs) was threaded through and glued with epoxy to a 230um core, 1.25mm diameter zirconia multimode ferrule (Precision Fiber Products), polished and cut at ~4mm for implantation. They were then tested for light output (~80-90% light recovery) and clean scoring of the fiber, and then each implant was numbered and the percent light recovery was noted for calibration of output for behavioral experiments. For surgical implantation, mice were anesthetized with 100mg/kg ketamine and 10mg/kg xylazine, and placed in a stereotaxic frame (Kopf). Mice were implanted bilaterally with sterile, chronically dwelling optical fibers targeted to the DG (dorsal implants: +/-1mm ML -1.5mm AP, -1.7mm DV, ventral implants: +/-2.5mm ML +/-3.7mm AP, -2mm DV). Optical fibers were secured with anchoring screws and dental cement. After surgery, mice were returned to their home cage and monitored until recovery from surgery. 3 weeks after surgery, before beginning behavioral testing mice were habituated to being attached to the patch cable by handling and attaching to the cable via a zirconia sleeve, and allowed to explore a novel cage for 15 min with no light for two consecutive days.

Induction of transgene expression and immunohistochemistry.

All mice were induced at 8 weeks of age and immunohistochemical analysis was conducted 6 weeks after TMX induction. For all experiments, mice were perfused (transcardial PBS, 4% paraformaldehyde), brains postfixed, cryoprotected, and sections (35 μ m) of the entire DG were collected. Primary antibodies were: chicken anti-green fluorescent protein (chicken anti-GFP; 1:500, Abcam, goat anti-doublecortin (DCX; 1:500, Santa Cruz Biotechnology), rabbit anti-Ki67 (1:100, Vector), rabbit anti-cFos (Millipore, ABE457, 1:1000) and mouse anti-NeuN, 1:1500, Millipore) (Kheirbek et al., 2013; Kheirbek et al., 2012; Sahay et al., 2011).

For induction of transgene expression in Nestin-CreER^{T2} mice, 8 week-old male mice were injected with 3mg tamoxifen (TMX) (VEH solution of corn oil/10%ethanol) I.P./day for 5 consecutive days. Testing began 6 weeks after the last TMX induction, as described in the text. In the DG of *Nestin^{Arch}*, *Nestin^{ChR2}* and *Nestin^{tdTomato}* mice, the majority of DCX+ cells expressed ChR2 or Arch, respectively (n=3-4/geno, *Nestin^{ChR2}*: 85.4+/- 2.9%, *Nestin^{Arch}*: 88.9 +/- 2.9%, *Nestin^{tdTomato}* 89.5+/- 3.8% of the DCX population of immature cells).

For immunohistochemical characterization of ChR2-eYFP⁺ and Arch-GFP⁺ cells in the Nestin-CreERT2 and tdTomato+ cells in imaged mice, confocal stacks (FluoView1000; Olympus) of DG sections were taken at 40x. For characterization of ChR2-eYFP⁺ and Arch-GFP⁺ cells, six sections across the DV axis of the DG (~400um between sections) were used for sampling cell number. For characterizing tdTomato+ cells, two sections spanning the implant site were taken for each hemisphere to compare implanted vs unimplanted side. For cell counting, the total number of labeled cells were counted in the GCL of the dentate gyrus and this number was divided by the sample volume (area was measured by tracing Hoescht stained to sections using ImageJ and multiplied by section thickness (35 μ m) to generate volume measurements) to generate cell density. For calculating recombination efficiency, 100 DCX cells were counted along the dorsoventral axis. These cells were then classified as positive or negative for tdTomato (in imaged mice), eYFP (in ChR2 mice) or GFP (in Arch mice). For the morphological analysis of immature neurons, z-stack images of tdTomato+ cells were traced and imported into Adobe Illustrator CS5 where neurons were reconstructed using the tracing tool. Images of the reconstructed neurons were opened in Fiji (<http://fiji.sc/Fiji>) where Sholl analysis was conducted using the Sholl analysis plug-in with parameters previously described (Sahay et al, 2011a). For calculating Ki67 number in implanted mice, six sections across the DV axis of each hemisphere DG (~400um between sections) were counted.

To sample the phenotypes of opsins/reporter positive cells in NestinCreER^{T2} mice, 35 μ m sections were cut through the DG of *Nestin^{ChR2}* mice, and two sections/mouse (~1200 mm between sections, one dorsal and one medioventral section) were imaged by taking confocal stacks at 40x. To calculate the percentage of ChR2-eYFP⁺ cells that expressed Ki67, DCX or NeuN, the total eYFP⁺ cells in 300 um x 200 um region of interest in the upper blade of the DG were counted in the green channel, and then in the red channel the number of eYFP⁺ cells immunoreactive for DCX, Ki67 or NeuN was counted. Characterization of the ChR2-eYFP positive cells 6 weeks after induction by co-staining for developmental stage markers demonstrated that 12.1 ± 0.4% (n = 3 mice) expressed Ki67 (i.e. were mitotic or recently mitotic), 52.2 ± 2.5% (n = 4 mice) were DCX-positive (i.e. were proliferating progenitor cells, neuroblasts or immature, <3 week-old, neurons) and 67.7 ± 4.1% (n = 3 mice) expressed NeuN (i.e. were neurons >2 weeks of age).

For assessing activity in the DG following window implantation, window implanted mice were placed in an open field box and allowed to explore for 20 min (as described below) and sacrificed 60 min after exploration. 50 μ m sections were cut along the entire AP axis of the hippocampus, and every 6th section was stained for cFos and counts of cFos+ nuclei in the GCL were taken (dorsal DG).

Dentate gyrus granule cell imaging

In vivo 2-photon imaging:

We used the same imaging system as described previously (Kaifosh et al., 2013; Lovett-Barron et al., 2014), with the addition of an 8kHz resonant galvanometer (Bruker). Approximately 150-250 mW of laser power was used during imaging, with adjustments in power levels to accommodate varying window clarity. To optimize light

transmission, we adjusted the angle of the mouse's head using two goniometers (Edmund Optics, +/-10 degree range) such that the imaging window was parallel to the objective. All images were acquired with a Nikon 40X NIR water-immersion objective (0.8 NA, 3.5 mm WD) in distilled water. We continuously acquired red (tdTomato) and green (GCaMP6f) channels separated by an emission cube set (green, HQ525/70m-2p; red, HQ607/45m-2p; 575dcxr, Chroma Technology) at 1024 x 1024 pixels covering 300 μ m x 300 μ m at 15 Hz with photomultiplier tubes (green GCaMP fluorescence, GaAsP PMT, Hamamatsu Model 7422P-40; red tdTomato fluorescence, multi-alkali PMT, Hamamatsu R3896). A custom dual stage preamp (1.4 x 10^5 dB, Bruker) was used to amplify signals prior to digitization.

Training:

Mice were water-restricted (>90% pre-deprivation weight) and trained to run on a cue-deplete burlap treadmill belt for water rewards over the course of 1-2 weeks. We applied a progressively restrictive water reward schedule, with mice initially receiving 40 randomly placed rewards per lap and ultimately receiving 3 randomly placed rewards per lap. Mice were trained for 20 minutes daily until they regularly ran at least one lap per minute. Mice were also habituated to the optical instrumentation (presence of objective, laser, shutter sounds) prior to imaging experiments.

Contexts:

Similar to our previous work, each context (1 and 2) consisted of the same treadmill belt (the same sequence of 3 joined fabric ribbons), but distinct in their visual, auditory, tactile, and olfactory stimuli (Fig 4A) (Lovett-Barron et al., 2014). During imaging sessions, mice received three randomly placed water rewards per lap, with reward positions changing randomly each lap. To allow for comparison of GC activity between similar contexts, the same three fabrics were used in the same order, but the locations of all of the tactile cues were shuffled between the two belts.

Stimulus presentation and behavioral readout:

Visual, auditory, and olfactory stimuli were presented and behavioral data were recorded as described previously (Kaifosh et al., 2013; Lovett-Barron et al., 2014). In order to reliably track the position of the treadmill belt, we established registration anchors at known positions along the belts and interpolated between them using a quadrature encoded movement signal tied to the rotation of the treadmill wheels. Registration anchors were marked by radio-frequency identification (RFID) buttons (16mm, 125kHz, SparkFun Electronics) at evenly spaced positions along the belt, and were read off as they passed over a fixed RFID reader (ID-12LA, SparkFun). The rotational quadrature signal was produced by marking treadmill wheels with offset tick marks, and this signal was encoded by a pair of photodiodes (SEN-0024, SparkFun) aligned to the wheels (<0.5cm resolution).

Calcium data processing:

All imaging data were analyzed using the SIMA software package (Kaifosh et al., 2014). Motion correction was performed using a 2D Hidden Markov Model (Dombeck et al., 2007; Kaifosh et al., 2013), with modifications to accommodate the specific features of data acquired with resonant galvanometers. These modifications have been made freely available with the latest versions of SIMA. Only the green GCaMP channel was used for estimating motion artifacts. In cases where motion artifacts were not adequately corrected, the affected data was discarded from further analysis. The especially sparse activity of dentate granule cells prevented the successful application of activity-based segmentation methods. Therefore, we used the SIMA project's ROI Buddy graphical user interface (Kaifosh et al., 2014) to draw regions of interest (ROIs) over GC somata visible in the time-averaged image of the motion-corrected green/GCaMP6f channel. We also used this software to determine the correspondence of ROIs across datasets from different trials in which the same FOV was imaged. To prevent the introduction of any bias, the red tdTomato channel was not viewed when drawing ROIs, but only referenced after all ROIs had been drawn in order to tag ROIs over tdTomato expressing cells as newborn GCs.

Dynamic GCaMP6f fluorescence signals were extracted from ROIs using SIMA according to the previously described formulation (Kaifosh et al., 2014). We then computed the relative fluorescence changes ($\Delta F/F$) (as described in (Jia et al., 2011)), with uniform smoothing window $t_1 = 3$ sec. and baseline size $t_2 = 60$ sec. We detected statistically significant calcium transients as described previously (Dombeck et al., 2007; Lovett-Barron et al., 2014). In order to improve our sensitivity, we then recalculated the baseline of the raw signal after masking

frames identified previously as occurring during a significant transient. $\Delta F/F$ was then recalculated, and transients re-estimated. Transients less than one second were removed to reduce false positives. This iterative procedure was repeated three times and effectively removed the transient contamination from the calculated baseline.

Spatial tuning vector and tuning specificity p-value analysis:

When evaluating the spatial tuning of GCs, we restricted our analysis to running-related epochs, defined as consecutive frames of forward locomotion (defined as an imaging frame in which at least one forward pair of beam breaks occurred) at least 1 sec in duration and with a minimum peak speed of 5 cm/sec. Consecutive epochs separated by < 0.5 seconds were merged. Running-related transients were defined as those that were initiated during a running-related epoch. Transient start was defined as the first imaging frame with mean fluorescence $\geq 2\sigma$, with σ equal to the standard deviation of the baseline frames. Offset was defined as the first frame with mean fluorescence $\leq 0.5\sigma$ (Dombeck et al. 2007). The spatial tuning vector was calculated as $\sum_j \frac{e^{i\theta_j}}{o(\theta_j)}$, where θ_j is the position of the mouse at the onset time of the j-th running-related transient, and o_j is the fraction of running frames acquired at position θ_j . In order to assess the significance of the spatial selectivity, for each cell we generated a null tuning distribution by shuffling the transient onset times (restricted to running frames) and repeatedly recomputing the tuning specificity. This process was repeated 100,000 times, and the p-value was defined as the fraction of this distribution that exceeded the GC's tuning specificity.

Spatial information p-value analysis:

For each cell we first computed the spatial information content (Skaggs, et al., 1993) as $I_N = \sum_{i=1}^N \lambda_i \ln \frac{\lambda_i}{\lambda} p_i$ where λ_i and p_i are the transient rate and fraction of time spent in the ith bin, λ is the overall firing rate, and N is the number of bins. We computed I_N for multiple values of $N = 2, 4, 5, 8, 10, 20, 25$, and 100. We then created 100,000 random reassessments of the transient onset times within the running-related epochs and re-computed the values of I_N^s , where s is the index of the shuffle. To roughly correct for biases in the calculation of mutual information, we then subtracted the mean of this null distribution from all estimates to obtain values $\hat{I}_N = I_N - \frac{1}{100,000} \sum_{s=1}^{100,000} I_N^s$. Finally, we computed a single estimate of the information content for the true transient onset times, $\hat{I} = \max_N \hat{I}_N$, and for the shuffles, $\hat{I}_s = \max_N \hat{I}_N^s$. The spatial tuning p-value was taken as the fraction of values of s for which \hat{I} exceeded \hat{I}_s .

Remapping analysis:

Rate maps were formed by dividing the number of transients starting in each bin by the occupancy of that bin. We calculated rate maps with 100 position bins and smoothed with a Gaussian kernel $\sigma=3$ bins). The tuning curve correlation for each cell was defined as the Pearson correlation coefficient between tuning curves for a cell in the two sequential context exposures. The centroid shift for each cell was defined as the angle (in radians) between the tuning directions calculated for the two context exposures. For both metrics, the shuffle distributions were calculated by estimating the tuning curve correlations or tuning shifts when cells were paired by a sub-sampled Cartesian product of cell identities (1000 pairs per shuffle).

Behavioral testing

Optogenetic modulation

In Arch experiments, the patch cables were interfaced to an FC/PC rotary joint (Doric lenses), which was attached on the other end to a 593.5 nm laser diode that was controlled by a Master-8 stimulator (AMPI). During the light on epoch, yellow light was provided for the full 5 min at a light power of 10mw at the tip of the implanted fiber optic. For ChR2 experiments, the hardware configuration was identical to the Arch experiments with the exception that illumination was provided by a 473nm laser diode (OEM). During the light on epoch, mice received blue light illumination for the full 5 min at 10hz, 20 ms pulses at a light power of 8 mw at the tip of the implanted fiber.

Open field test

Mice were quickly attached to the fiber optic patch cables (bilaterally) via a zirconia sleeve, then placed in an open-field chamber 22.1" wide x 22.1" long x 15.83" high (Kinder Scientific) with high lux illumination (600lux). Sessions lasted for 15 min consisting of three 5 min epochs: light off, light on, and light off. Data was collected and analyzed with *MotorMonitor* software, and total distance traveled and percent of that distance traveled in the center of the arena was documented.

Elevated plus maze

Hardware configuration and experimental protocols for EPM were identical to OFT (15min session, 5min light off/on). Mice were placed in the closed arm of the open field and allowed to explore the maze. Sessions were videotaped, and the videos were analyzed for time spent in closed arms, open arms and center of the maze using *TopScan* software (Clever Sys).

Fear conditioning:

Hardware configuration and light intensity was identical to OFT and EPM, stimulation epochs are presented in the text. Different cohorts of mice were used for each test, thus littermate controls were used for each experiment to control for differences in genetic background. Conditioning took place in Coulbourn Instruments fear conditioning boxes that contained one clear plexiglass wall, three aluminum walls and a stainless steel grid as a floor. Mice were brought in to the testing room in a novel cage, attached to the fiber optic patch cables then placed in fear conditioning boxes. The training session began with the onset of the houselight and fan, and anise scent was placed under the grid floor. In this one-trial contextual fear conditioning protocol, mice received light stimulations as described in the text, and 180 s after placement of the mouse in the training context and onset of houselight and fan, mice received single 2-s foot shock of 0.75 mA. All freezing was measured before the single footshock. The mouse was taken out 15 s after termination of the foot shock and returned to its home cage. The grid and the waste tray were cleaned Sani-Cloths® HB Germicidal Disposable Wipes (Orangeburg, NY) between runs. Mice were recorded by digital video cameras mounted above the conditioning chamber, and were scored for freezing by an investigator blind to the genotype of the animal.

Contextual fear discrimination:

Conditioning took place in the same Coulbourn fear conditioning boxes as above. For training in context A mice were brought into the testing room in an novel cage with novel bedding on the floor. The training context (A) included a houselight and fan, and anise scent was placed under the grid floor. Mice were exposed to the context, then after 180s, they received single 2s foot shock of 0.75mA. Mice were taken out 15s after termination of the foot shock and returned to their home cage. The box was cleaned with Sanicloths between runs. For exposure to the similar (no-shock) context, B, mice were brought into the testing room in transport buckets by the same experimenter who had handled the mice for the training context. Context B shared many features of the training context, A, including an exposed stainless steel grid floor, but differed in that two plastic inserts were used to cover the walls and make them circular, the house fan and lights were turned off, and the chamber door was left ajar during testing. A lemon scent was used as an olfactory cue, and 70% ethanol was used to clean the grids between runs. Mice were run first in context B, then after 2h, mice were placed in the training context A. As the shock was given at the end of context A, all freezing in both contexts was assessed before animals were shocked. Measurement of the freezing levels (by an experimenter blind to treatment condition) in both the training context (3-min pre-shock) and the similar context (3min) each day allowed the assessment of freezing in the two contexts.

For the dissimilar context, C, the grid floor was covered with a plastic panel and cage bedding. The chamber walls were covered and made circular using plastic inserts, the house fan and lights were turned off, and a mild lemon scent was placed below the grid floor. The chamber door was left ajar during testing. 70% ethanol used to clean the chamber between runs. Mice were run first in context C, then after 2hr were run in context A. As above, the shock was given at the end of context A, ensuring that all freezing measured in both contexts was assessed before animals were shocked. Measurement of the freezing levels in both the training context (3-min pre-shock) and the novel context (3min) each day allowed the assessment of freezing in the two contexts.

Statistics

For all optogenetic behavioral data, data was analyzed using ANOVA with repeated measurements where appropriate. All tests are described in the appropriate figure legends. Group numbers were based on previous optogenetic and 2-photon imaging experiments(Kheirbek et al., 2013; Lovett-Barron et al., 2014). For imaging data, for all normally distributed data, a Welch's two-sample T-Test was used for comparison of means with n-1 degrees of freedom. The Mann-Whitney U Test was used for comparison of means in non-normally distributed data with n-1 degrees of freedom. A paired student's T-Test was used for comparison of means in paired data with n-1 degrees of freedom. The one-sided Kolmogorov-Smirnov (KS) test was used for testing the hypothesis that a distribution was drawn from an underlying theoretical distribution with n-1 degrees of freedom (uniformity in the case of Fig 2E and 4D). The two-sided two-sample Kolmogorov-Smirnov test with n-1 degrees of freedom was used for testing the null hypothesis that two empirical distributions were drawn from the same continuous underlying distribution.

Supplementary references

- Dombeck, D.A., Khabbaz, A.N., Collman, F., Adelman, T.L., and Tank, D.W. (2007). Imaging large-scale neural activity with cellular resolution in awake, mobile mice. *Neuron* *56*, 43-57
- Dranovsky, A., Picchini, A.M., Moadel, T., Sisti, A.C., Yamada, A., Kimura, S., Leonardo, E.D., and Hen, R. (2011). Experience dictates stem cell fate in the adult hippocampus. *Neuron* *70*, 908-923
- Jia, H., Rochefort, N.L., Chen, X., and Konnerth, A. (2011). In vivo two-photon imaging of sensory-evoked dendritic calcium signals in cortical neurons. *Nature protocols* *6*, 28-35
- Kaifosh, P., Lovett-Barron, M., Turi, G.F., Reardon, T.R., and Losonczy, A. (2013). Septo-hippocampal GABAergic signaling across multiple modalities in awake mice. *Nat Neurosci* *16*, 1182-1184
- Kaifosh, P., Zaremba, J.D., Danielson, N.B., and Losonczy, A. (2014). SIMA: Python software for analysis of dynamic fluorescence imaging data. *Frontiers in neuroinformatics* *8*, 80
- Kheirbek, M.A., Drew, L.J., Burghardt, N.S., Costantini, D.O., Tannenholz, L., Ahmari, S.E., Zeng, H., Fenton, A.A., and Hen, R. (2013). Differential control of learning and anxiety along the dorsoventral axis of the dentate gyrus. *Neuron* *77*, 955-968
- Kheirbek, M.A., Tannenholz, L., and Hen, R. (2012). NR2B-dependent plasticity of adult-born granule cells is necessary for context discrimination. *The Journal of neuroscience : the official journal of the Society for Neuroscience* *32*, 8696-8702
- Lovett-Barron, M., Kaifosh, P., Kheirbek, M.A., Danielson, N., Zaremba, J.D., Reardon, T.R., Turi, G.F., Hen, R., Zemelman, B.V., and Losonczy, A. (2014). Dendritic inhibition in the hippocampus supports fear learning. *Science* *343*, 857-863
- Madisen, L., Mao, T., Koch, H., Zhuo, J.M., Berenyi, A., Fujisawa, S., Hsu, Y.W., Garcia, A.J., 3rd, Gu, X., Zanella, S., et al. (2012). A toolbox of Cre-dependent optogenetic transgenic mice for light-induced activation and silencing. *Nat Neurosci* *15*, 793-802
- Madisen, L., Zwingman, T.A., Sunkin, S.M., Oh, S.W., Zariwala, H.A., Gu, H., Ng, L.L., Palmiter, R.D., Hawrylycz, M.J., Jones, A.R., et al. (2010). A robust and high-throughput Cre reporting and characterization system for the whole mouse brain. *Nat Neurosci* *13*, 133-140
- Sahay, A., Scobie, K.N., Hill, A.S., O'Carroll, C.M., Kheirbek, M.A., Burghardt, N.S., Fenton, A.A., Dranovsky, A., and Hen, R. (2011). Increasing adult hippocampal neurogenesis is sufficient to improve pattern separation. *Nature* *472*, 466-470